Inorganic Chemistry

pubs.acs.org/IC

Article

Systematic Variation of 3d Metal Centers in a Redox-Innocent Ligand Environment: Structures, Electrochemical Properties, and Carbon Dioxide Activation

Niklas W. Kinzel, Derya Demirbas, Eckhard Bill, Thomas Weyhermüller, Christophe Werlé, Nicolas Kaeffer,* and Walter Leitner*

Cite This: *Inorg. Chem.* 2021, 60, 19062−19078

Read Online

ACCESS | Metrics & More | Article Recommendations | Supporting Information

ABSTRACT: Coordination compounds of earth-abundant 3d transition metals are among the most effective catalysts for the electrochemical reduction of carbon dioxide (CO_2). While the properties of the metal center are crucial for the ability of the complexes to electrochemically activate CO_2, systematic variations of the metal within an identical, redox-innocent ligand backbone remain insufficiently investigated. Here, we report on the synthesis, structural and spectroscopic characterization, and electrochemical investigation of a series of 3d transition-metal complexes [M = Mn(I), Fe(II), Co(II), Ni(II), Cu(I), and Zn(II)] coordinated by a new redox-innocent PNP pincer ligand system. Only the Fe, Co, and Ni complexes reveal distinct metal-centered electrochemical reductions from M(II) down to M(0) and show indications for interaction with CO_2 in their reduced states. The Ni(0) d^{10} species associates with CO_2 to form a putative Aresta-type Ni-η^2-CO_2 complex, where electron transfer to CO_2 through back-bonding is insufficient to enable electrocatalytic activity. By contrast, the Co(0) d^9 intermediate binding CO_2 can undergo additional electron uptake into a formal cobalt(I) metallacarboxylate complex able to promote turnover. Our data, together with the few literature precedents, single out that an unsaturated coordination sphere (coordination number = 4 or 5) and a d^7-to-d^9 configuration in the reduced low oxidation state (+I or 0) are characteristics that foster electrochemical CO_2 activation for complexes based on redox-innocent ligands.

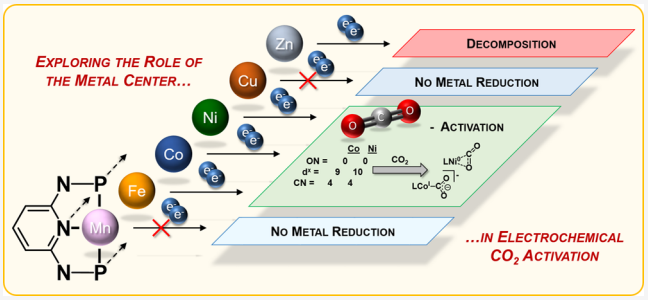

1. INTRODUCTION

Closing the anthropogenic carbon cycle constitutes a pivotal challenge to tackle climate change and provide humankind with the necessary carbon-based materials in a defossilized future.[1] In this context, the catalytic conversion of carbon dioxide either taken from industrial waste streams or ultimately drawn from the atmosphere poses a powerful tool.[2,3] Turning the chemically inert CO_2 molecule into a C_1 building block accessible for further transformation (e.g., copolymerization,[4−6] hydrogenation,[7−9] electro-/photochemical reduction[10,11] or synthesis,[12,13] and combinations thereof[14,15]) is a promising strategy toward that aim. The thermodynamic challenge of this approach can be virtuously addressed in supplying the required energy for the conversion of CO_2 by renewable electricity. To overcome the kinetic barriers, molecular complexes of earth-abundant 3d transition metals are heavily investigated, ranging among the most effective and efficient electrochemical CO_2 reduction (eCO_2R) catalysts.[10,16] In a recent literature survey, we analyzed the main reaction pathways of homogeneously catalyzed CO_2 electroreduction from an organometallic perspective. We classified them into mechanisms traversing the direct coordination and activation of CO_2 to the metal center (electron transfer through a molecular complex, ET_M) and those requiring the previous formation of a metal hydride (electron transfer through hydride, ET_H) as the reactive intermediate (Figure 1).[17]

The intrinsic characteristics of the metal center, such as hydricity[18−22] or substrate (CO_2) and product (CO, HCO_2H, etc.) binding affinity,[23] define the prevailing mechanistic route, which is directly linked to the catalytic performance. However, only a limited number of studies report on the systematic variation of the metal center within an identical ligand framework in relation to CO_2 electroreduction (Figure 2A).[24−27] The majority of these studies rely on the so-called "noninnocent" ligands because these ligands are often perceived as beneficial for the activity by sharing excess electron density (redox noninnocence) or relaying protons

Received: September 17, 2021
Published: December 1, 2021

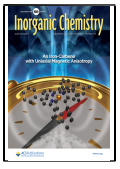

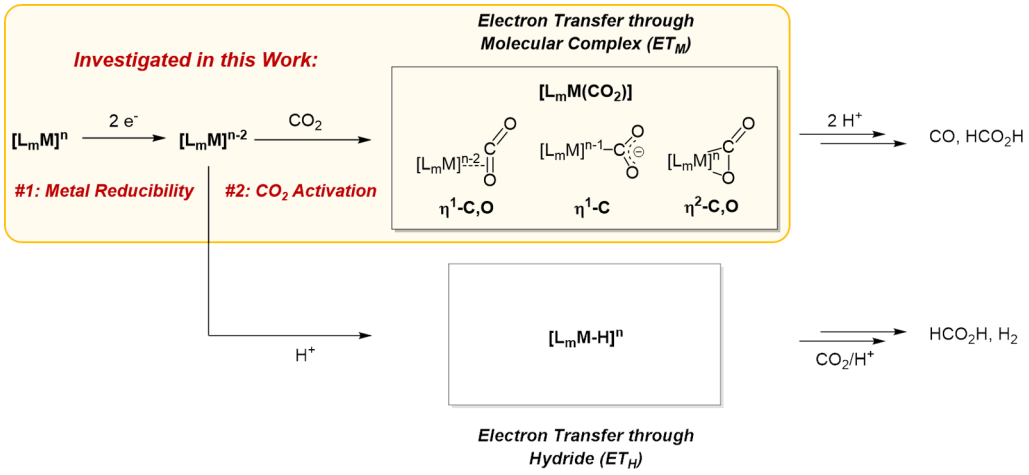

Figure 1. Electron transfers during transition-metal-catalyzed electroreduction of CO_2: ET_M and ET_H pathways (M = metal, L = ligand, m = stoichiometry of coordinated ligands, and n = formal oxidation state of the metal).

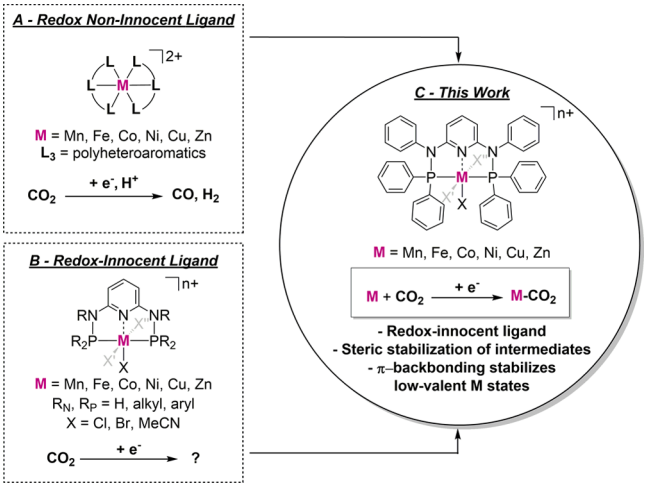

Figure 2. (A) Studies investigating 3d metal series in the same noninnocent ligand frameworks,[25,27] (B) complexes reported in the literature coordinated by redox-innocent PN_3P ligand frameworks,[32−38] and (C) focus of this work.

(chemical noninnocence).[28−30] The resulting complex interplay of ligand- and metal-centered processes renders deconvolution of the individual contributions rather challenging.[31] By contrast, systematic variations of the metal centers with redox-innocent ligands, such as pincer platforms,[32−39] remain insufficiently investigated in the frame of CO_2 electroreduction (Figure 2B).

In the present study, we thus investigated the structural and electrochemical properties toward CO_2 conversion of 3d transition-metal complexes based on an identical "innocent" ligand framework. We purposely aimed at involving a ligand inert to redox and protonation processes under common electrocatalytic conditions (Figure 2C) and therefore designed the new PNP ligand **L** (Figure 3). The ligand displays a large steric demand to shield the metal center and a high degree of aromaticity, which we surmised would only marginally interfere in the redox processes but still provide sufficient π-back-bonding ability to stabilize low-valent metals. We report the synthesis, structural, and spectroscopic characterizations of a series of complexes comprising mid-to-late 3d transition metals (Mn to Zn) coordinated by this pincer-type ligand platform. The redox properties of the complexes were then studied, employing cyclic voltammetry (CV) to probe the reducibility of the core metal (requisite #1 in Figure 1). We then investigated the most promising set of complexes (Fe, Co, and Ni) toward electrochemical activation of the CO_2 substrate (requisite #2 in Figure 1). We specifically focus this study on the metal−CO_2 interaction as the entry into an electrocatalytic CO_2 reduction cycle along the ET_M pathway (highlighted in Figure 1) by depriving the system of protons to hinder the ET_H route.

2. RESULTS

2.1. Synthesis and Structural Characterization.

2.1.1. N^2,N^6-Bis(diphenylphosphanyl)-N^2,N^6-diphenylpyridine-2,6-diamine (L). Ligand **L** was prepared following a two-step synthesis route (Figure 3).

In the first step, 2,6-dibromopyridine and aniline were reacted following a reported palladium-catalyzed Buchwald−Hartwig coupling to produce N^2,N^6-diphenylpyridine-2,6-diamine,[40] which was isolated in 76% yield after purification by column chromatography on silica. Subsequently, diphenylphosphino moieties were installed by low-temperature lithiation of the diamine in tetrahydrofuran (THF) before

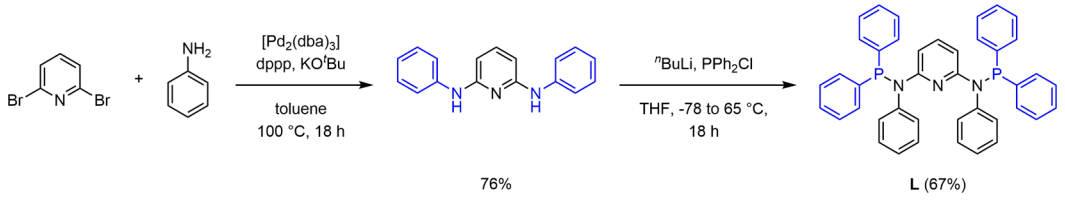

Figure 3. Synthesis of **L**.

https://doi.org/10.1021/acs.inorgchem.1c02909
Inorg. Chem. 2021, 60, 19062−19078

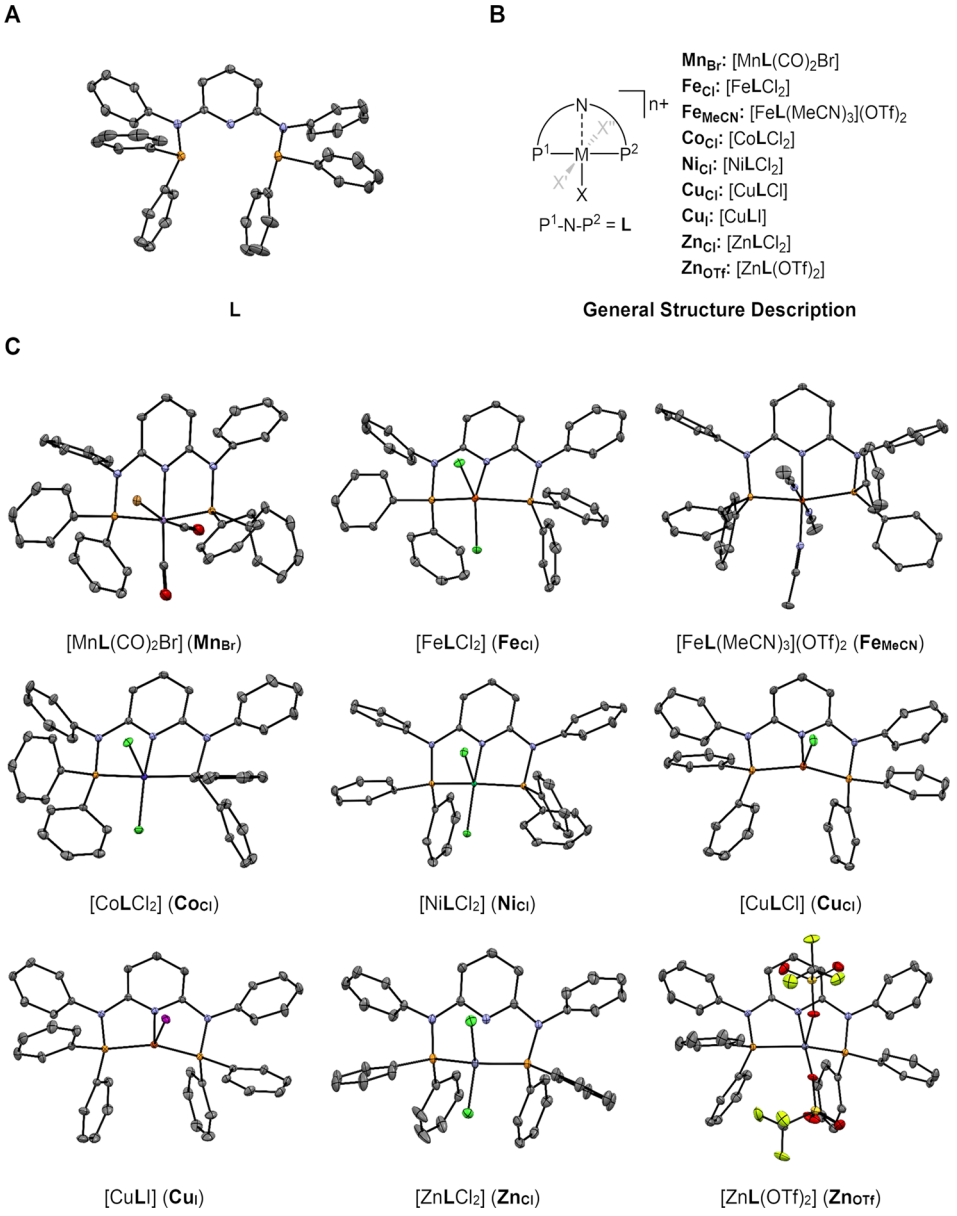

Figure 4. (A) Molecular structure of **L**, (B) general structure description, and (C) molecular structures of the complexes $\mathbf{M_X}$ investigated in this study. H atoms, outer-sphere ligands, and cocrystallized solvent molecules were omitted for clarity; thermal ellipsoids are shown at the 50% probability level. For $\mathbf{Mn_{Br}}$, the major *cis*-CO configuration is presented. Color code: gray, C; blue, N; red, O; yellow, F; orange, P; green, Cl; brown, Br; pink, I.

the addition of chlorodiphenylphosphine and stirring at 65 °C for 18 h. NMR spectroscopic analysis (Figures S1−S3), high-resolution mass spectrometry (HRMS), and elemental analysis confirmed the structure and purity of ligand **L** received in 67% yield after workup (detailed synthetic procedures are given in the Experimental Section).

Even before the coordination of a metal atom, the molecular structure of the ligand (Figure 4A) exhibits the typical pincer shape, with the five atoms forming the PN_3P pincer belt nearly coplanar (PNCN torsion angles at 8.0° and −15.4°). This planarity might result from a steric hindering of the rotation around the C−N bond linking the pyridine core and the bulky aniline moiety or from conjugation of the lone pairs of the aniline N atoms with the heterocycle, inferring in-plane triangular geometry at these N atoms. We also note that the *pinching* character of **L** is marked with a relatively short P−P distance (d_{P-P} = 4.226 Å), likely by virtue of the steric constraint imposed at the aniline N atoms, making the C−N−P angles narrow (119.5° and 115.7°).

Pincer transition-metal complexes were obtained by the metalation of **L** with 3d transition-metal precursors in yields ranging from 52 to 95%, as indicated in the Experimental Section. Schematic structures of the resulting $\mathbf{M_X}$ complexes (where M = metal center and X = inner-sphere coordinating unit regardless of the stoichiometry) are presented in Figure 4B.

For a systematic comparison, we first targeted pincer complexes bearing metal centers in their +II oxidation state and bis-chloride coordination. These structures were successfully obtained for Fe ($\mathbf{Fe_{Cl}}$), Co ($\mathbf{Co_{Cl}}$), Ni ($\mathbf{Ni_{Cl}}$), and Zn ($\mathbf{Zn_{Cl}}$) but remained elusive for Mn and Cu (*vide infra*). In these cases, complexes $\mathbf{Mn_{Br}}$ and $\mathbf{Cu_{Cl}}$ were derived from the

https://doi.org/10.1021/acs.inorgchem.1c02909
Inorg. Chem. 2021, 60, 19062−19078

Table 1. Selected Bond Distances (Å) and Angles (deg) as well as Structural Parameters τ and Idealized Coordination Geometries for the Complexes in this Study

	M−N	M−P^1	M−P^2	P^1−M−N	P^1−M−P^2	τ_4	τ_5[41]	idealized geometry
Mn$_{Br}$	2.0391(13)	2.2623(5)	2.2273(5)	83.22(4)	166.305(18)			O_h
Fe$_{Cl}$	2.3269(10)	2.4260(3)	2.4291(3)	73.77(2)	130.409(13)		0.38	SBP
Fe$_{MeCN}$	1.9717(9)	2.2411(3)	2.2238(3)	83.67(3)	167.824(12)			O_h
Co$_{Cl}$	1.9465(10)	2.1882(4)	2.1847(4)	84.90(3)	166.277(14)		0.04	SBP
Ni$_{Cl}$	1.9084(11)	2.1407(4)	2.1574(4)	85.26(3)	155.509(15)		0.23	SBP
Cu$_{Cl}$	2.1377(8)	2.2556(3)	2.2687(3)	80.89(2)	135.982(11)	0.78		T_d
Cu$_{I}$	2.1283(7)	2.2299(2)	2.2589(2)	78.69(19)	133.215(9)	0.77		T_d
Zn$_{Cl}$	2.7383(9)[a]	2.4489(3)	2.4182(3)	64.50(2)[a]	112.597(11)	0.95		T_d
Zn$_{OTf}$	2.335(2)	2.3979(8)	2.3758(8)	72.38(6)	129.09(3)		0.82	TBP

[a]No bond between the metal and N.

Mn(CO)$_5$Br and CuCl precursors, respectively, in their +I oxidation state. Along with these complexes, we also made variations to less electronegative or more weakly coordinating anions and prepared **Fe$_{MeCN}$**, **Cu$_I$**, and **Zn$_{OTf}$**.

Single crystals could be obtained for **L** and each of the **M$_X$** complexes, allowing elucidation of their molecular structures by X-ray diffraction (XRD), as represented in Figure 4C.

Characteristic features of the structures (Figure 4C), calculated structural parameters and coordination geometries (Table 1), and selected NMR spectroscopic data (Table 2) will be discussed for each species individually in the following sections.

Table 2. ^{31}P NMR (δ_P) and Coordination ($\Delta\delta$) Chemical Shifts, ^{1}H NMR Chemical Shifts of the Pyridinic Protons in the Meta Position [δ_H(PyH_m); CD_2Cl_2, 500 MHz, 296 K] for Complexes in this Study, and Spin S for Paramagnetic Complexes in this Study

	δ_P (ppm)	$\Delta\delta$ (ppm)	δ_H(PyH_m) (ppm)[a]	S
L	52.8		5.81 (8.0)	
Mn$_{Br}$	138.9	86.1	5.79 (8.2)	
Fe$_{Cl}$			57.14 (−)	2
Fe$_{MeCN}$	129.2	76.4	5.99 (8.2)	
Co$_{Cl}$				$^1/_2$
Ni$_{Cl}$	85.0	32.2	5.73 (8.2)	
Cu$_{Cl}$	39.9	−12.9	5.68 (8.0)	
Cu$_{I}$	40.0	−12.8	5.67 (8.0)	
Zn$_{Cl}$	30.9	−21.9	5.85 (8.1)	
Zn$_{OTf}$	28.8	−24.0	5.94 (8.2)	

[a]$^3J_{doublet}$ (Hz) indicated in parentheses.

2.1.2. [MnL(CO)$_2$Br]. In the case of Mn, metalation with $MnCl_2$ at room temperature (rt) in THF, as reported for related pyridine-based PNP pincers (R_N = H; R_P = ^{i}Pr),[37] did not succeed with our ligand nor did other variations in the conditions (solvents, temperatures, precursors, etc.). The only reported [Mn(PN$_3$P)Cl$_2$] structure within a pyridine-based pincer framework displays an almost ideal square-based-pyramidal (SBP) geometry (τ_5 = 0.04) with two P atoms in the trans position of the basal plane and relatively distant from Mn (d_{Mn-P} = 2.574 and 2.590 Å and d_{P-P} = 4.886 Å), in a high-spin, five-unpaired-electron configuration ($\mu_{eff} \approx 6$).[37] We surmise that **L** does not allow such significant elongation between the two P atoms, likely required in a putative [MnLCl$_2$] complex. The electron-withdrawing character of the phenyl substituent at the P atom may also disfavor the coordination of a Mn(II) fragment.

By contrast, coordination of the Mn^I(CO)$_5$Br precursor effectively yields the Mn(I) complex **Mn$_{Br}$**, suggesting stabilization of the lower oxidation state by **L**. This 18-electron Mn complex crystallizes in a distorted octahedral (O_h) coordination environment, as is commonly encountered for related pincer manganese(I) carbonyl bromide complexes.[42] In this particular case, XRD analysis revealed a mixture of the cis and trans configurations of the CO ligands in a 95:5 ratio in the crystal.

The diamagnetic d^6 low-spin **Mn$_{Br}$** complex exhibits distinguishable, but overlapping sets of ^{1}H NMR signals for the chemically inequivalent aromatic protons of the R_N and R_P phenyl moieties positioned syn or anti of Br in the predominant *cis*-CO configuration (Figure S4).

2.1.3. [FeLCl$_2$]. **Fe$_{Cl}$** crystallizes in a strongly distorted SBP structure, as reflected by a τ_5 value of 0.38. The PNP coordination sites of **L** exhibit relatively extended bond distances of 2.327 Å for Fe−N as well as 2.429 and 2.426 Å for both Fe−P bonds. Interestingly, the steric demand of the R_N = Ph group in **L** seems to prevent the formation of bis-PN$_3$P-coordinated species, which readily occurs for R_N = H.[33]

Although ^{1}H NMR analysis of **Fe$_{Cl}$** in CD_2Cl_2 exhibits the contact-shifted peaks diagnostic of a paramagnetic Fe(II) center, signals at 57.50 and −11.79 ppm are assigned by integration to pyridinic protons in the meta and para positions, respectively, and indicate a high level of symmetry in the structure (Figure S7).

The zero-field ^{57}Fe Mössbauer spectrum of **Fe$_{Cl}$** recorded with a powder sample at 80 K showed a quadrupole doublet with high isomer shift, δ = 0.80 mm·s^{-1}, and large quadrupole splitting, ΔE_Q = 3.33 mm·s^{-1} (Figure S32). The values are typical of high-spin Fe(II) with S = 2. Accordingly, the compound was electron paramagnetic resonance (EPR)-silent in a THF solution at X-band frequencies [because the zero-field splitting of the quintet state exceeds the microwave quantum energy, as is often encountered for the 3d^6 configuration of Fe(II)]. Moreover, the effective magnetic moment of solid **Fe$_{Cl}$** was μ_{eff} = 4.9 μ_B at 270 K (Figure S35), in agreement with the spin-only value expected for S = 2. The axial zero-field splitting parameter obtained from the temperature variation of the magnetic susceptibility χT versus temperature T is in the usual range for Fe(II), S = 2 with D = 4 cm^{-1}.

In the 3d^6 high-spin electronic configuration of Fe(II) in **Fe$_{Cl}$**, the highest occupied molecular orbital (HOMO) is a $d_{x^2-y^2}$ one, which is expected to be stabilized by distortion of the SBP structure to high θ_{apic} angle values (up to 117°).[43] Similar distorted SBP geometries were observed on a series of

https://doi.org/10.1021/acs.inorgchem.1c02909
Inorg. Chem. 2021, 60, 19062−19078

related PN_3P-coordinated iron bis-chloride complexes, for which extended Fe−N and Fe−P distances were related to a high-spin state at Fe.[34]

2.1.4. [FeL(MeCN)$_3$]Cl$_2$ and [FeL(MeCN)$_3$](OTf)$_2$. Dissolving $\mathbf{Fe_{Cl}}$ in acetonitrile (MeCN; e.g., for CV analysis) results in a color change from yellow to red (for UV/vis spectra see Figure S31), indicative of a substantial change in the coordination sphere. Corroborating this point, new diamagnetic signals build up between 5.6 and 8.0 ppm in ^{1}H NMR spectra taken in CD_3CN.

To further elucidate the identity of the formed species, we assessed the structure of an $\{Fe^{II}\mathbf{L}\}^{2+}$ fragment in MeCN by reacting in this solvent the ligand **L** with the $Fe(OTf)_2$ precursor bearing weakly coordinating anions. The resulting $\mathbf{Fe_{MeCN}}$ complex exhibits a distorted octahedral geometry, where **L** occupies three meridional positions of the inner coordination sphere, completed by three MeCN ligands. The P^1−Fe−N bond angles are close to the expected 90° for the two axial solvent ligands (91.40 and 89.75°) but are significantly distorted for the equatorial MeCN (98.56°), as is also reported for Fe(II) PN_3P tris-MeCN complexes (R_N = H; R_P = Ph).[32] ^{1}H NMR analysis of $\mathbf{Fe_{MeCN}}$ (Figure S11) revealed equatorial and axial MeCN signals (2.43 and 1.73 ppm, integration 1:2) in CD_2Cl_2 and the disappearance of these signals by exchange with the deuterated solvent in CD_3CN (Figure S14). The Mössbauer spectrum of solid $\mathbf{Fe_{MeCN}}$ showed a significantly lower isomer shift than $\mathbf{Fe_{Cl}}$ with δ = 0.34 mm·s^{-1}, as well as weak quadrupole splitting of 0.87 mm·s^{-1} (Figure S33). These parameters readily exclude a high-spin configuration but reveal a diamagnetic d^6 low-spin configuration of $\mathbf{Fe_{MeCN}}$ with S = 0, as was already inferred from the NMR response.

Comparing the NMR spectra of $\mathbf{Fe_{Cl}}$ in CD_3CN with that of an authentic $\mathbf{Fe_{MeCN}}$ sample in the same solvent points to identical coordination environments. The conversion of $\mathbf{Fe_{Cl}}$ in MeCN was further supported by crystals grown from an MeCN solution of $\mathbf{Fe_{Cl}}$ that reveal an inner-sphere molecular structure (Figure S37) identical with that of $\mathbf{Fe_{MeCN}}$.

Further NMR studies yet showed that the conversion of $\mathbf{Fe_{Cl}}$ into $\mathbf{Fe_{MeCN}}$ in MeCN is incomplete in solution; the two species are in equilibrium with other intermediates (Figure S9). We, therefore, use $\mathbf{Fe_{MeCN}}$ for further electrochemical analysis in MeCN to analyze a single well-defined species.

2.1.5. [CoLCl$_2$]. $\mathbf{Co_{Cl}}$ coordinates in an almost ideal SBP structure with τ_5 very close to zero. For comparison, with R_N = H, Rösler et al. reported a structure also resembling the ideal SBP (τ_5 = 0.01).[36] $\mathbf{Co_{Cl}}$ displays a bond length of 239 pm between Co and the apical (apic) chloride atom (241 pm for the example by Rösler et al.[36]), which suggests that this ligand is only weakly bound. However, crystals prepared from the strongly coordinating MeCN solvent (Figure S38) showed neither formation of the outer-sphere chlorido complex nor substitution of the ligand by a solvent molecule but only a fractional elongation of the Co−Cl_{apic} bond to 242 pm.

$\mathbf{Co_{Cl}}$ exhibits heavily broadened ^{1}H NMR signals in the 5−12 ppm chemical shift region (Figure S15) that are in accordance with a paramagnetic d^7 electron configuration. Although integration of the peaks sums to the expected 33 protons, the paramagnetic character of the substance prohibited further NMR spectroscopic analysis on other nuclei.

Solid $\mathbf{Co_{Cl}}$ gave an effective magnetic moment of 1.9 μ_B at 270 K (Figure S36), consistent with the spin-only value for S = $^1/_2$ (1.73 μ_B) and in line with related complexes in the literature (an effective magnetic moment of 2.3 μ_B was reported for R_N = H).[36] The corresponding $3d^7$ low-spin configuration of $\mathbf{Co_{Cl}}$ was further corroborated by the X-band EPR spectrum of the compound in an MeCN solution at 10 K, showing distinct anisotropic g splitting and ^{59}Co hyperfine splitting (Figure S34).

We posited that the nearly ideal SBP geometry observed for $\mathbf{Co_{Cl}}$ is favored over distortions to higher values of τ_5 because the corresponding structures would stabilize the singly occupied d_{z^2} orbital but concomitantly destabilize the fully occupied d_{yz} and d_{xz} orbitals.[43]

2.1.6. [NiLCl$_2$]. $\mathbf{Ni_{Cl}}$ displays an SBP structure, with a distortion intermediate of $\mathbf{Fe_{Cl}}$ and $\mathbf{Co_{Cl}}$. Electronic stabilization of the d_{z^2} HOMO procured by a θ_{apic} value of up to 110°[43] is particularly favorable for the 18-electron d^8 configuration of $\mathbf{Ni_{Cl}}$. Here, the apical chlorido ligand is weakly bound to the metal as well, manifesting in a bond length of 255 pm. Although the formation of a cationic almost ideally square-planar (SP) d^8 [Ni(PN_3P)Br]Br complex (with R_N = H) was observed in methanol (MeOH),[32] $\mathbf{Ni_{Cl}}$ crystals grown from MeCN (Figure S39) maintain the apical chlorido ligand coordinated with a marginally elongated bond distance.

NMR spectroscopy revealed a ^{31}P singlet peak at 85.0 ppm (Figure S18) and well distinguished sets of ^{1}H signals (Figure S16) for the different aromatic positions, most indicative for the pyridinic protons in the meta position that exhibit a characteristic doublet at 5.73 ppm (J = 8.2 Hz; Table 2).

2.1.7. [CuLCl] and [CuLI]. For Cu, the reaction of **L** with $CuCl_2$ produced a diamagnetic complex, as inferred from NMR analysis, whereas a putative monomeric [Cu**L**Cl_2] complex would be paramagnetic (d^9). We suspect *in situ* reduction of Cu(II) to Cu(I) upon coordination to **L** with simultaneous oxidation of the ligand (additional diamagnetic signals in the ^{1}H and ^{31}P{^{1}H} spectra), as was already reported in the literature.[44−47] We thus aimed for the Cu(I) complex $\mathbf{Cu_{Cl}}$, which could be successfully synthesized starting directly from CuCl. The identical NMR spectra and crystal structures (data not shown) of the products synthesized from $CuCl_2$ and CuCl supported this approach. Similarly, $\mathbf{Cu_I}$ was synthesized from CuI to introduce the less electronegative iodo ligand.

The tetracoordinated d^{10} complexes both exhibit a distorted tetrahedral (T_d) structure, with τ_4 values of 0.78 (chloride) and 0.77 (iodide) being intermediate between that of the ideal tetrahedron (τ_4 = 1) and that of a butterfly/seesaw structure (τ_4 ≈ 0.43). The coordination geometries found are in accordance with known bromide analogues (R_N = Me; τ_4 = 0.78).[35]

NMR spectroscopic analysis (Figures S19−S24) reflects the similar coordination structure, with the ^{31}P peaks (39.9 and 40.0 ppm for $\mathbf{Cu_{Cl}}$ and $\mathbf{Cu_I}$, respectively) and ^{1}H peaks [e.g., 5.68 ppm (J = 8.0 Hz) and 5.67 ppm (J = 8.0 Hz) for PyH_m in $\mathbf{Cu_{Cl}}$ and $\mathbf{Cu_I}$, respectively] only marginally deviating (Table 2).

2.1.8. [ZnLCl$_2$] and [ZnL(OTf)$_2$]. In $\mathbf{Zn_{Cl}}$, the pyridine unit is not bound to the metal center, in contrast to the shared behavior of the earlier $\mathbf{M(II)_{Cl}}$ complexes, leaving the complex in an almost ideal tetrahedral coordination geometry (τ_4 = 0.95). The 18-electron valence of this d^{10} configuration at the Zn center likely favors tetracoordinated structures over pentacoordinated structures. $\mathbf{Zn_{Cl}}$ preferentially adopts a tetrahedral structure over a SP one, possibly because HOMOs in the former (t_2 orbitals) are significantly more stabilized than the HOMO in the latter (b_{1g} orbital).

https://doi.org/10.1021/acs.inorgchem.1c02909
Inorg. Chem. 2021, 60, 19062−19078

Additionally, the structural constraints of the pincer ligand might disfavor formation of the SP configuration. A bromide analogue with R_N = Me also exhibits the tetrahedral structure.[38]

By contrast, $\mathbf{Zn_{OTf}}$ retains pentacoordination and forms a 20-valence electron (VE) complex of distorted trigonal-bipyramidal (TBP) structure, as reflected in the τ_5 value of 0.82. 20-electron complexes are only accessible in very weak field complexes, where the antibonding molecular orbital hosting two electrons is sufficiently low in energy, with the TBP geometry stabilized compared to SBP.[43] $\mathbf{Zn_{OTf}}$ is the only example of a pyridine-based PNP pincer complex derived from the $Zn(OTf)_2$ precursor to the best of our knowledge. Therefore, the closest relatable system is the terpyridine (tpy)-coordinated Zn complex reported by Bocian et al., which crystallizes in a seesaw/butterfly structure (τ_5 = 0.47).[48] Here, the bond between Zn and the N atom of the pyridine core is significantly shorter than the Zn−N bond in $\mathbf{Zn_{OTf}}$ (204 vs 233 pm), indicating that the N is loosely coordinated in the latter system.

Distinctions in the molecular structures of $\mathbf{Zn_{Cl}}$ and $\mathbf{Zn_{OTf}}$ also can be seen in the recorded NMR spectra (Figures S25−S30), with a difference of 2.1 ppm for the ^{31}P nucleus (30.9 and 28.8 ppm for $\mathbf{Zn_{Cl}}$ and $\mathbf{Zn_{OTf}}$, respectively) and 0.09 ppm [5.85 ppm (J = 8.1 Hz) and 5.94 ppm (J = 8.2 Hz) for $\mathbf{Zn_{Cl}}$ and $\mathbf{Zn_{OTf}}$, respectively] for the meta protons of the pyridine unit.

2.2. Electrochemical Analysis under an Ar Atmosphere. The electrochemical behaviors of **L** and $\mathbf{M_X}$ will be discussed individually in this section. The cyclic voltammograms under an Ar atmosphere of the $\mathbf{M_{Cl}}$ complexes bearing chlorido ligands and $\mathbf{Fe_{MeCN}}$ are depicted in Figure 5. The potentials of the redox events derived thereof are summarized in Table 3.

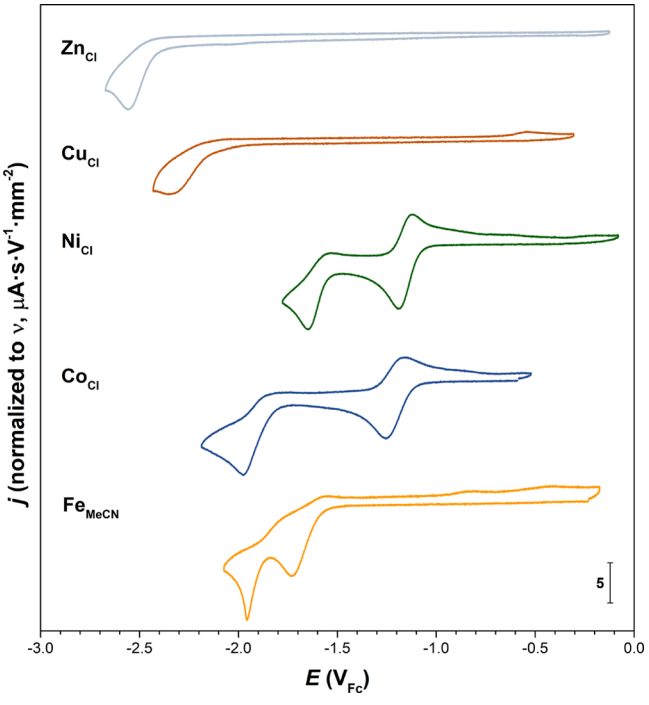

Figure 5. Cyclic voltammograms of selected complexes investigated in this study under an Ar atmosphere ([$\mathbf{M_X}$] = 1 mM, MeCN, 0.1 M ^{n}Bu$_4$NPF$_6$, glassy carbon working electrode, and ν = 100 mV·s^{-1}).

Table 3. Redox Potentials of the Complexes Investigated in This Study under an Ar Atmosphere[a]

	$M^{II/I}$			$M^{I/0}$			ligand
	$E^0/E_{p,c}$ (V_{Fc})	I/R	ΔE_p (mV)	$E^0/E_{p,c}$ (V_{Fc})	I/R	ΔE_p (mV)	$E_{p,c}$ (V_{Fc})
$\mathbf{Mn_{Br}}$[b]							−2.64
$\mathbf{Fe_{MeCN}}$	−1.73	I		−1.96	I		
$\mathbf{Co_{Cl}}$	−1.21	R	94	−1.98	I		−2.61
$\mathbf{Ni_{Cl}}$	−1.16	R	69	−1.59[d]	R	114	−2.41
$\mathbf{Cu_{Cl}}$	−0.09	R	130				−2.35
$\mathbf{Cu_{I}}$	−0.03	R	128				−2.27
$\mathbf{Zn_{Cl}}$							−2.56
$\mathbf{Zn_{OTf}}$	−1.86[c]	I					−2.94

[a][$\mathbf{M_X}$] = 1 mM, MeCN, 0.1 M ^{n}Bu$_4$NPF$_6$, glassy carbon working electrode, and ν = 100 mV·s^{-1}; E^0 values are reported for reversible (R) waves and $E_{p,c}$ for irreversible (I) waves. [b]Recorded in DMF because of the poor solubility in MeCN. [$\mathbf{Mn_{Br}}$] = 0.5 mM. [c]Likely $Zn^{II/0}$ reduction. [d]At ν = 5 V·s^{-1}.

2.2.1. Ligand L. **L** was found to be electrochemically inert in the window of potentials from −2.5 to −0.1 V versus $Fc^{+/0}$ (abbreviated V_{Fc} in the following) in MeCN and *N*,*N*-dimethylformamide (DMF; Figure S40), thus falling in the category of redox-innocent systems.

2.2.2. [MnL(CO)$_2$Br]. $\mathbf{Mn_{Br}}$ shows an irreversible reduction wave at $E_{p,c}$ = −2.64 V_{Fc} (Figure S41) in CV. For related Mn complexes [Mn(tpy)(CO)$_2$Br][49] (tpy = 2,2′:6′,2″-terpyridine) bearing the tris-chelating planar tpy ligand, a metal-centered reduction to a Mn(0) species with concomitant halide loss and subsequent fast dimerization was suggested. Nevertheless, the lack of an anodic wave for the reoxidation of a putative dimer of reduced $\mathbf{Mn_{Br}}$ makes such a metal-centered reduction event appear unlikely. In addition, $\mathbf{Mn_{Br}}$ is already in an 18-VE, alleged d^6 low-spin configuration, and reduction would populate a high-lying e_g orbital. We therefore propose that reduction is centered on the ligand at the strongly cathodic potential observed here (Figure 6A).

2.2.3. [FeL(MeCN)$_3$](OTf)$_2$. $\mathbf{Fe_{MeCN}}$ exhibits two narrowly separated irreversible cathodic waves at $E_{p,c}$ = −1.73 and −1.96 V_{Fc} (Figure 5), which we attribute to the $Fe^{II/I}$ and $Fe^{I/0}$ reductions, respectively, accompanied by chemical steps, viz., the loss of MeCN ligands and major structural changes. The corresponding back-oxidation waves are only visible at scan rates (ν) higher than 20 V·s^{-1}, suggesting that follow-up chemical events are fast. The occurrence of structural reorganization upon reduction is also supported by the observation of a reoxidation wave at a considerably more positive potential ($E_{p,a}$ = −1.24 V_{Fc}) that follows reversal of the potential scan between the first and second reduction waves (Figure S44). This oxidation wave vanishes at low scan rates when the scan is reversed after the second reduction wave (Figure S45). We thus suggest that $\mathbf{Fe_{MeCN}}$ reduces to a $[Fe^{I}\mathbf{L}(MeCN)_n]^+$ complex (n = 3), which undergoes fast MeCN loss into short-lived $[Fe^{I}\mathbf{L}(MeCN)_n]^+$ with n = 1 or 2 (Figure 6B). Further evolution of this Fe(I) intermediate likely generates a dimeric $[Fe^{I}_2\mathbf{L}_2(MeCN)_{2n}]^{2+}$ compound, in the form of an Fe−Fe-bonded or an MeCN-bridged one. We tentatively attribute the oxidation wave at −1.24 V_{Fc} to the oxidation of such dimeric species. The second reduction wave is then assigned to reduction of the putative $[Fe^{I}_2\mathbf{L}_2(MeCN)_{2n}]^{2+}$ dimer into an $[Fe^{0}_2\mathbf{L}_2(MeCN)_{2n'}]$ species. When the scan reversal is negative to this second

https://doi.org/10.1021/acs.inorgchem.1c02909
Inorg. Chem. 2021, 60, 19062−19078

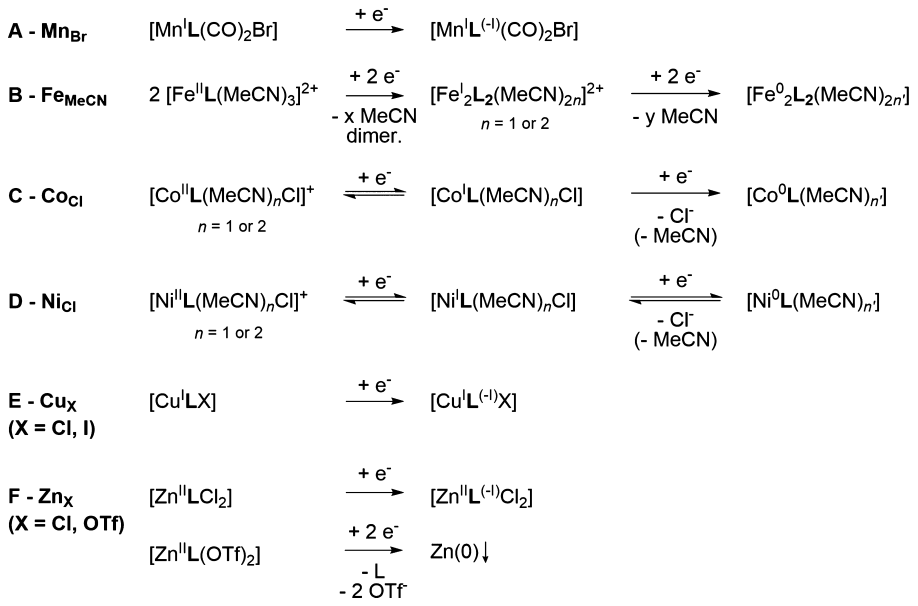

Figure 6. Proposed (electro)chemical steps for the reduction of complexes investigated in this study under an Ar atmosphere.

reduction, the disappearance of the reoxidation wave at −1.24 V_{Fc} for low sweep rates suggests the evolution of the postulated [Fe$^0_2$L$_2$(MeCN)$_{2n'}$] dimer into monomeric Fe(0) species or other degradation products [e.g., Fe(0) deposits]. The reversibility of the second reduction wave is gradually established when the scan rate is raised (from 5 V·s^{-1}), corresponding to reoxidation of the transient Fe(0) complex, from which the follow-up chemical step is only moderately fast.

2.2.4. [CoLCl$_2$]. In the cyclic voltammogram of **Co$_{Cl}$** (Figure 5), a partially reversible reduction wave at E^0 = −1.21 V_{Fc} (ΔE_p = 94 mV) and an irreversible wave at $E_{p,c}$ = −1.98 V_{Fc} can be observed, to which we assign the Co$^{II/I}$ and Co$^{I/0}$ couples, respectively. Although the molecular structure obtained for **Co$_{Cl}$** from an MeCN solution confirmed the inner-sphere coordination of both chlorido ligands in the solid state, we hypothesize that a dynamic ligand exchange between Cl$^-$ and MeCN takes place in solution.[50] Likely, a cationic [Co^{II}L(MeCN)$_n$Cl]$^+$ (n = 1 or 2) complex forms upon the dissolution of **Co$_{Cl}$** into MeCN. We postulate that the complex reversibly reduces into a neutral [Co^{I}L(MeCN)$_n$Cl] species (Figure 6C). Further reduction of the Co(I) complex then proceeds concomitantly with a chemical event in an electrochemical−chemical (EC) sequence. The Co$^{I/0}$ wave remaining irreversible even at high sweep rates (up to 100 V·s^{-1}; Figure S48) suggests that the follow-up chemical step is fast. We attribute this fast chemical step to the dissociation of a chloride ligand, forming a putative [Co^{0}L(MeCN)$_{n'}$] complex.

2.2.5. [NiLCl$_2$]. **Ni$_{Cl}$** shows a voltamperometric pattern at 100 mV·s^{-1} similar to that of **Co$_{Cl}$** with a reversible reduction wave at E^0 = −1.16 V_{Fc}, followed by an irreversible process at a more negative potential of $E_{p,c}$ = −1.65 V_{Fc} (Figure 5), to which we respectively assign the Ni$^{II/I}$ and Ni$^{I/0}$ events. With a weakly coordinated apical chlorido ligand in the solid state, we postulate that, similar to **Co$_{Cl}$**, **Ni$_{Cl}$** exchanges in a MeCN solution with a cationic [Ni^{II}L(MeCN)$_n$Cl]$^+$ (n = 1 or 2) complex. The reduction of [Ni^{II}L(MeCN)$_n$Cl]$^+$ is proposed to generate a neutral [Ni^{I}L(MeCN)$_n$Cl] species (Figure 6D). As stems from the irreversibility of the Ni$^{I/0}$ event, the formation of a Ni(0) species is here also coupled to a chemical step (EC), likely a Cl$^-$ elimination producing a low-valent [Ni^{0}L(MeCN)$_{n'}$] complex. In that case, however, the reversibility of the Ni$^{I/0}$ couple can be recovered by elevating the scan rate (Figure S50), suggesting a slow chemical step. A standard potential of E^0(Ni$^{I/0}$) = −1.59 V_{Fc} is recovered from the reversible wave at a fast scan rate. The $E_{p,c}$ versus log(ν) graph decays linearly in the irreversibility region (*KP*, *pure kinetics* zone of the kinetic zone diagram) with a −22.1 mV·dec^{-1} slope (Figure S51), in reasonable agreement with the theoretical value for an EC mechanism expected at −29.6 mV·dec^{-1}.[51] From this data, the apparent forward rate constant $k_{f,app}$ of the coupled chemical step was estimated at $k_{f,app}$(Ar) = 3.6 × 10^{-1} s^{-1}.

Two more negative irreversible reduction waves appear at $E_{p,c}$ = −2.41 and −2.75 V_{Fc} (Figure S42). We assign the wave at −2.41 V_{Fc} to a ligand-centered reduction, but the second reduction wave has remained unassigned so far.

2.2.6. [CuLCl] and [CuLI]. **Cu$_{Cl}$** exhibits an irreversible reduction wave at $E_{p,c}$ = −2.35 V_{Fc} (Figure 5). At first sight, the irreversibility of the wave may be explained by Cu(I) to Cu(0) reduction with concomitant loss of the halide. While putative Cu(0) complexes are expected to decompose into heterogeneous Cu(0) deposits at the electrode surface, no substantial oxidative desorption peak commonly accounting for the oxidation of such Cu(0) deposits could be observed in the backward reaction of the investigated potential window, regardless of the scan rate. Therefore, we propose that the reduction wave relates to a reduction centered at the ligand rather than at the metal (Figure 6E). Moreover, a reversible Cu$^{II/I}$ oxidation wave can be observed at −0.09 V_{Fc} (Figure S43). Referring to the challenging synthesis of the Cu(II) species, it is interesting that the +II oxidation state apparently can be accessed by electrochemical means. The Cu(II) complex is possibly only stable in the time scale of the CV experiment and decomposes during the reaction time of the synthesis.

Cu$_I$ shows almost identical redox features compared to **Cu$_{Cl}$** with an irreversible reduction wave at $E_{p,c}$ = −2.27 V_{Fc} (Figure S41), which we assume is a ligand-centered reduction as well (Figure 6E) and a reversible wave at E^0 = −0.03 V_{Fc} assigned to a Cu$^{II/I}$ couple (Figure S43).

https://doi.org/10.1021/acs.inorgchem.1c02909
Inorg. Chem. 2021, 60, 19062−19078

2.2.7. [ZnLCl$_2$] and [ZnL(OTf)$_2$]. An irreversible reduction wave was found for $\mathbf{Zn_{Cl}}$ at $E_{p,c}$ = −2.56 V_{Fc}. d^{10} Zn ions are usually redox-innocent in accessible reduction windows, and the corresponding complexes are thus commonly used to identify the redox behavior of the coordinated ligand system.[52−54] In particular, $\mathbf{Zn_{Cl}}$ is already in a stable 18-electron configuration with metal 3d orbitals fully occupied (d^{10}), making a metal-centered reduction unlikely. We therefore posited that the reduction observed at low potential is centered on the ligand (Figure 6F).

The cathodic scan of $\mathbf{Zn_{OTf}}$ displays a reduction wave at $E_{p,c}$ = −1.86 V_{Fc} (Figure S41), whose trace is crossed by that of the backward anodic scan and followed by a sharp oxidative desorption peak at higher potential ($E_{p,a}$ = −0.79 V_{Fc}). The observation of a line crossing and a desorption wave is diagnostic of electrodeposition upon reduction. Therefore, we assume that the reduction wave of $\mathbf{Zn_{OTf}}$ represents a two-electron reduction to Zn(0) with concomitant decomposition in (nanoparticulate) deposits on the electrode surface (Figure 6F). Solution dissociation of $\mathbf{Zn_{OTf}}$ into a dicationic complex would rationalize the positive shift in the reduction potential compared to $\mathbf{Zn_{Cl}}$.

2.2.8. Proposed (Electro)chemical Steps upon the Reduction of M_X Complexes. The proposed electrochemical and chemical steps traversed by the presented complexes upon reduction in CV are summarized in Figure 6.

Because $\mathbf{Fe_{MeCN}}$, $\mathbf{Co_{Cl}}$, and $\mathbf{Ni_{Cl}}$ exhibit distinct metal-centered reduction waves, which is a prerequisite for an ET_M mechanism in CO_2 reduction, the electrochemical behavior of these complexes was analyzed further in the presence of CO_2.

2.3. Electrochemical Analysis under a CO_2 Atmosphere. The cyclic voltammograms under a CO_2 atmosphere for $\mathbf{Fe_{MeCN}}$, $\mathbf{Co_{Cl}}$, and $\mathbf{Ni_{Cl}}$ are reported in Figure 7. The shifts in the potential of the two metal-centered reduction waves upon switching of the gases $\Delta E_{p,c}^{Ar\rightarrow CO_2}$ are summarized in Table 4.

Under a CO_2 atmosphere, $\mathbf{Fe_{MeCN}}$ exhibits potentials shifted cathodically by approximately −20 and −100 mV for the $M^{II/I}$ and $M^{I/0}$ couples, respectively, compared to data under an Ar atmosphere. Moreover, at a scan rate of 100 V·s^{-1}, the reversibility of the two metal-centered waves is not retained to the extent observed under an Ar atmosphere (Figures S46 and S47). With a focus on the second reduction wave, a noticeable change in the reaction mechanism is observable from the change in the peak shape. While dimer formation is likely under Ar atmosphere, this pathway might be inhibited by the coordination of CO_2 at this stage.

For $\mathbf{Co_{Cl}}$, the $Co^{II/I}$ redox wave remains unaffected by CO_2, discarding the reaction with this substrate at the Co(II) and Co(I) states. By contrast, the $Co^{I/0}$ irreversible wave shifts by approximately 50 mV in the anodic direction upon CO_2 saturation. This observation evidences CO_2 coordination upon the reduction to Co(0) in an EC mechanism. Even at elevated scan rates, the $Co^{I/0}$ wave remains irreversible (Figure S49), evidencing a fast CO_2 association rate. The lack of knowledge of $E_{Ar}^0(Co^{I/0})$ (*vide supra*) yet prevented quantification of the rate constant of CO_2 association under our electrochemical conditions. Interestingly, however, a slight increase in the cathodic peak current (ratio $j_{p,c}$ = 1.4) is also observed and suggests electrocatalytic activity. Although reductive disproportionation of CO_2 into CO and CO_3^{2-} is conceivable under the dry conditions used here, we suspect that traces of protons (from residual water or Hoffman degradation of the ^{n}Bu$_4$N$^+$ cation) are involved in the CO_2 electroreduction.

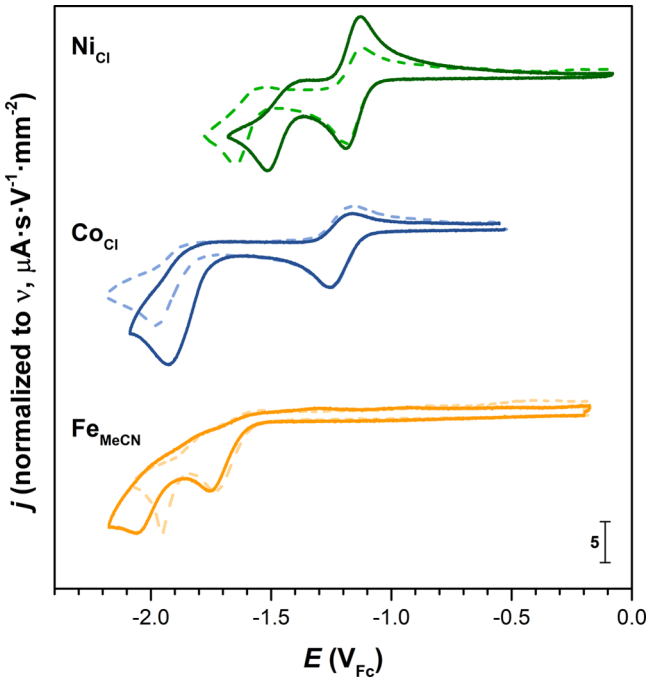

Figure 7. Cyclic voltammograms of selected complexes investigated in this study under Ar (dashed line) and CO_2 (full line) atmospheres ([$\mathbf{M_X}$] = 1 mM, MeCN, 0.1 M ^{n}Bu$_4$NPF$_6$, glassy carbon working electrode, and ν = 100 mV·s^{-1}).

Table 4. $\Delta E_{p,c}^{Ar\rightarrow CO_2}(M^{II/I})$ and $\Delta E_{p,c}^{Ar\rightarrow CO_2}(M^{I/0})$ for M_X under Ar and CO_2 Atmospheres[a]

	$\Delta E_{p,c}^{Ar\rightarrow CO_2}(M^{II/I})$ (mV)	$\Delta E_{p,c}^{Ar\rightarrow CO_2}(M^{I/0})$ (mV)
$\mathbf{Fe_{MeCN}}$	−20	−100
$\mathbf{Co_{Cl}}$	<10	50
$\mathbf{Ni_{Cl}}$	<10	130

[a][$\mathbf{M_X}$] = 1 mM, MeCN, 0.1 M ^{n}Bu$_4$NPF$_6$, glassy carbon working electrode, and ν = 100 mV·s^{-1}.

For $\mathbf{Ni_{Cl}}$, the $Ni^{II/I}$ couple is also left unaffected by CO_2, discarding coordination at the corresponding +II and +I oxidation states. On the contrary, $\mathbf{Ni_{Cl}}$ exhibits a very strong anodic shift (∼130 mV) at the $Ni^{I/0}$ wave under CO_2, the largest observed at the $M^{I/0}$ couples of the analyzed complexes. At variance with the observation under an Ar atmosphere, the reversibility of the $Ni^{I/0}$ reduction wave cannot be recovered by a faster scan rate (up to 100 V·s^{-1}; Figure S52). These observations mark a clear indication of a fast CO_2 association at the Ni(0) stage (EC). Corroborating this process, $E_{p,c}$ = $f[\log(\nu)]$ linearly decays by −38.7 mV·dec^{-1} in the *KP* zone (Figure S53). Prior knowledge of $E_{Ar}^0(Ni^{I/0})$ allows one to evaluate the CO_2 association apparent rate constant (section 2.2), found at $k_{f,app}(CO_2)$ = 4.2 × 10^3 s^{-1}, which gives a bimolecular rate constant of $k_{A,f}(CO_2)$ = 1.5 × 10^4 M^{-1}·s^{-1} (taking a saturation concentration at 1 atm of CO_2 of [CO_2] = 0.28 M in an MeCN solution[23]).

Furthermore, from scan rates above 10 V·s^{-1}, an additional oxidation wave ($E_{p,a}$ = −0.39 V_{Fc} for ν = 50 V·s^{-1}) becomes visible. We associate this anodic wave with the oxidation of a $[Ni^{II}\mathbf{L}(MeCN)_n(CO_2H)]^+$ or $[Ni^{II}\mathbf{L}(MeCN)_n(CO)]^{2+}$ (n = 1 or 2) adduct only accessible at elevated scan rates due to the limited lifetime of the species. We can, however, not fully

https://doi.org/10.1021/acs.inorgchem.1c02909
Inorg. Chem. 2021, 60, 19062−19078

exclude that this wave corresponds to the oxidation of a putative $[Ni^{II}L(MeCN)_nH]^+$ hydride species formed by the reaction of a Ni(0) intermediate with residual protons.

3. DISCUSSION

3.1. Structural and Spectroscopic Properties. The bond distances between the coordination sites and the donor atoms (P and N) of the ligand scaffold are depicted in Figure 8A. In the subgroup of SBP complexes $\mathbf{M_{Cl}}$ (M = Fe, Co, and Ni), the M−P and M−N bonds shorten while the 3d row is incremented, as expected from the decreasing metal ionic radii in the 3d block.[55] The trend is overruled as other factors such as the auxiliary ligands and coordination geometries are varied.

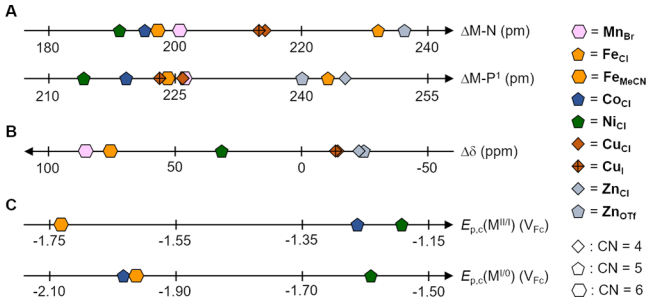

Figure 8. (A) Metal−ligand bond distances, (B) $\Delta\delta$ derived from $^{31}P\{^1H\}$ NMR spectra in CD_2Cl_2 ($\mathbf{Fe_{Cl}}$ and $\mathbf{Co_{Cl}}$ did not exhibit a ^{31}P signal due to the paramagnetic nature of these complexes), and (C) $E_{p,c}(M^{II/I})$ and $E_{p,c}(M^{I/0})$ of applicable complexes studied in this work.

The ^{31}P $\Delta\delta$ values, defined as the difference between the chemical shift of the free versus coordinated ligand (see the Supporting Information for details), show a systematic variation along with the metal series. The value decreases when the electron count is incremented from the left ($\mathbf{Mn_{Br}}$) to the right ($\mathbf{Zn_{Cl/OTf}}$) of the 3d row (Figure 8B). The observed trend is consistent with increasing electron density at the metal center within the same oxidation state when traversing from left to right in the 3d period. For the lowest 3d electron counts (Mn, Fe, and Ni), the predominant σ donation of the phosphine deshields the coordinated P and produces positive $\Delta\delta$ values, whereas the highest electron counts (Cu and Zn) induce an additional π-acceptor ability of the phosphine, resulting in negative $\Delta\delta$ values.

3.2. Metal-Based Reducibility. In the series of complexes under scrutiny, metal-centered reductions are generally prevented with a $3d^{10}$ configuration (viz., $\mathbf{Cu_{Cl/I}}$ and $\mathbf{Zn_{Cl}}$) likely because of the combined saturation of the 3d metal orbitals and the valence shell (Figure 9). The ligand only reduces at very negative potentials (below −2 V_{Fc}), irrespective of the metal center, confirming the redox-innocent nature of this ligand. Nevertheless, below these potentials, reduction of the ligand is possible.

Although deviating from a d^{10} configuration, the d^6 low-spin $\mathbf{Mn_{Br}}$ complex also exhibits a ligand-centered reduction event only. We posited that the strongly field-splitting carbonyl ligands destabilize the unoccupied e_g orbitals of the metal center to the extent where ligand reduction is energetically more favorable than metal reduction, although at very cathodic potentials (<−2.5 V_{Fc}). One may thus conclude that CO-coordinated Mn complexes generally require redox-active ligands (e.g., bipyridine[56]) or a cationic state[57] to be active in CO_2 electroreduction. This point is in sharp contrast to thermochemical CO_2 reduction passing through the Mn−H pathway, where manganese(I) carbonyl complexes based on redox-innocent ligands are highly efficient catalysts.[58−61]

M_X	d^x (VE)	CN (Geom.)	Electrochemical Behavior
Zn_{OTf}	d^{10} (20)	5 (TBP)	$M^{II/I}$ $M^{I/0}$ $L^{0/-I}$ Dec.
Zn_{Cl}	d^{10} (**18**)	4 (T_d)	$M^{II/I}$ $M^{I/0}$ $L^{0/-I}$ Dec.
$Cu_{Cl/I}$	d^{10} (**18**)	4 (T_d)	$M^{II/I}$ $M^{I/0}$ $L^{0/-I}$ Dec.
Ni_{Cl}	d^8 ls (**18**)	5 (SBP)	$M^{II/I}$ $M^{I/0}$ $L^{0/-I}$ Dec.
Co_{Cl}	d^7 ls (17)	5 (SBP)	$M^{II/I}$ $M^{I/0}$ $L^{0/-I}$ Dec.
Fe_{MeCN}	d^6 ls (**18**) ↑ MeCN	6 (O_h) ↑ MeCN	$M^{II/I}$ $M^{I/0}$ $L^{0/-I}$ Dec.
Fe_{Cl}	d^6 hs (16)	5 (SBP)	$M^{II/I}$ $M^{I/0}$ $L^{0/-I}$ Dec.
Mn_{Br}	d^6 ls (**18**)	6 (O_h)	$M^{II/I}$ $M^{I/0}$ $L^{0/-I}$ Dec.

Figure 9. Observed electronic/geometric properties and electrochemical behavior for the complexes in this study (Dec. = decomposition).

For complexes with lower ligand-field splitting, the deviation from the d^{10} state unlocks metal-centered reduction processes, as observed in the case of $\mathbf{Fe_{MeCN}}$, $\mathbf{Co_{Cl}}$, and $\mathbf{Ni_{Cl}}$ (Figure 9). Here we note that Fe, Co, and Ni complexes are among the most prominent eCO_2R catalysts.[17] While ligand-centered reductions at mildly negative potentials are commonly proposed for Fe, Co, or Ni complexes[17,25,30,31,50,62,63] (e.g., with polypyridinic ligands having delocalized, low-energy π^* orbitals), in our series, a comparison with the other complexes (of Mn, Cu, and Zn) allows assignment of the first two reductions (Figure 8C) solely to metal-centered orbitals in $\mathbf{Fe_{MeCN}}$, $\mathbf{Co_{Cl}}$, and $\mathbf{Ni_{Cl}}$.

3.3. Electrochemical CO_2 Activation. Complex $\mathbf{Fe_{MeCN}}$ shows an $Fe^{II/I}$ voltamperometric wave that is affected by the presence of CO_2 (although marginally), indicating coordination at the Fe(I) state. With $\mathbf{Fe_{MeCN}}$ adopting a distorted octahedral geometry in a d^6 low-spin configuration, the one-electron reduction from Fe(II) to Fe(I) populates an e_g antibonding orbital. In the presence of CO_2, the fast chemical step deduced from the irreversibility of the $Fe^{II/I}$ wave is consistent with the high reactivity of Fe(I) species. The activation of CO_2 at Fe(I) centers reported previously, namely, in eCO_2R, has been mainly observed with complexes bearing redox-active ligands,[64] which are thus best described as ligand-reduced Fe(II) complexes. For the redox-inactive pincer ligand used here, we postulate that the metal-centered radical binds CO_2 to form $[Fe^{I}L(MeCN)(CO_2)]^+$ as the primary intermediate. We note that one of the rare reported metal-centered Fe(I) radicals is known to result in the bimolecular cleavage of CO_2 into a (μ-CO)(μ-O)-bridged Fe(II) dimer[65] and a similar bimolecular CO_2 activation with $\mathbf{Fe_{MeCN}}$ also seems possible.

Moving from Fe to Co in $\mathbf{Co_{Cl}}$, CO_2 activation occurs only at the M(0) state instead of M(I). The slightly distorted SBP geometry determined for $\mathbf{Co_{Cl}}$ in the solid state is expected to be retained in an MeCN solution, possibly with chloride and solvent in dynamic exchange at the apical position. The HOMO is consequently a single occupied d_{z^2} one at the d^7 configuration of paramagnetic $\mathbf{Co_{Cl}}$. The first reduction is expected to fill this d_{z^2} orbital, producing a diamagnetic

https://doi.org/10.1021/acs.inorgchem.1c02909
Inorg. Chem. 2021, 60, 19062−19078

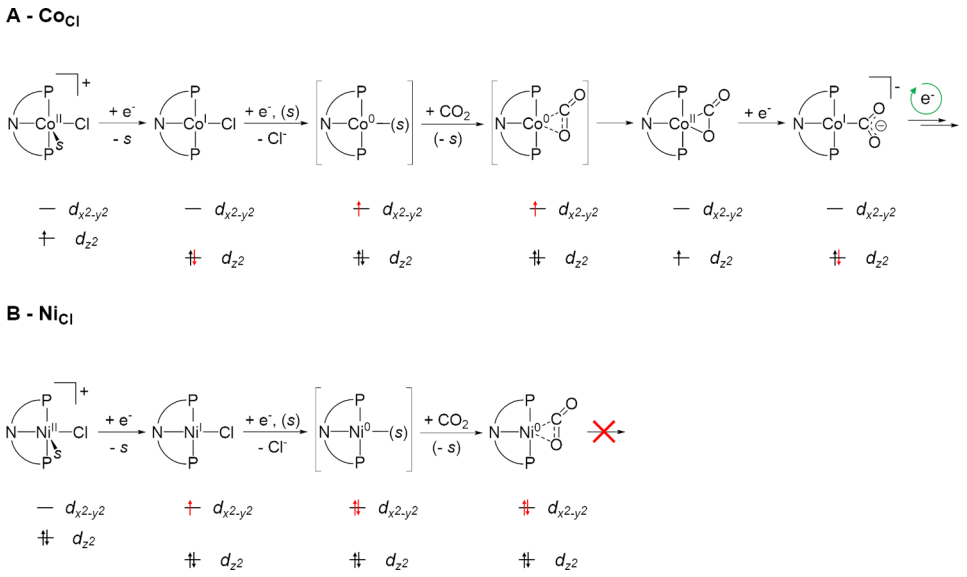

Figure 10. Proposed electrochemical pathways with schematic frontier orbital diagrams for the reduction of (A) **Co$_{Cl}$** and (B) **Ni$_{Cl}$** under a CO_2 atmosphere (s = MeCN).

[Co^I**L**(MeCN)Cl] complex (Figure 10A). Release of the apical ligand would stabilize the now fully occupied d_{z^2} orbital in a SP [Co^I**L**Cl] 16-electron complex, as found for the related pincer complex [Co^I(PN$_3$P)(MeCN)]$^+$ (R_N = H; R_P = ^{t}Bu).[66] The large potential gap to the second reduction in a Co(0) species [$E_{p,c}$(Co$^{I/0}$) − E^0(Co$^{II/I}$) = −670 mV] is consistent with the need for the injection of a second electron into a high-lying antibonding $d_{x^2-y^2}$ orbital. This second reduction is followed by an irreversible chemical step (EC), most probably the expulsion of Cl$^-$ concomitant with MeCN association to generate a neutral [Co^0**L**(MeCN)] complex. Calculations on similar [Co^0(PNP)(MeCN)] complexes suggest a η^2 π-bonded MeCN in a structure best described as a cobalt(II) cycloimine.[66] We postulate that MeCN binding rather than Cl$^-$ expulsion is rate-determining. The positive shift of the irreversible Co$^{I/0}$ reduction (*pure kinetics* conditions, *KP*) under CO_2 indicates that the associated chemical equilibrium is more shifted or accelerated forward with that substrate. The electrophilic nature of the C atom of CO_2 likely makes the association faster compared to that of MeCN. Although formally metalloradicals, Co(0) species do not commonly exhibit single-electron-transfer reactivity but undergo two-electron oxidative chemistry.[67] We thus favor formulation of the CO_2 activation product as a d^7 [Co^{II}**L**(CO_2)] complex. The potential at which this intermediate is accessed is low enough for further reduction into a 16-electron [Co^I**L**(CO_2)]$^-$ complex, refilling the low-lying d_{z^2} orbital (Figure 10A). This feature would provide a direct entry into a catalytic cycle for CO_2 reduction, as supported by an increased magnitude of the current density at the Co$^{I/0}$ wave. We note, however, that the current enhancement observed in the presence of CO_2 may also result from a faradaic (and not catalytic) two-electron reduction from [Co^I**L**Cl] to [Co^I**L**(CO_2)]$^-$.

Complex **Ni$_{Cl}$** also displays a SBP coordination geometry and similar to Co interacts with CO_2 only at the 0 oxidation state. **Ni$_{Cl}$** is reduced down to a Ni(0) species by two consecutive electron injections expected to fill the $d_{x^2-y^2}$ orbital (Figure 10B), a fact corroborated by reduced states computed on a [Ni(PN$_3$P)Br$_2$] complex bearing a close PN$_3$P ligand (R_N = H or Me; R_P = Ph).[68] Compared to **Co$_{Cl}$**, the potential gap between the +I and 0 oxidation states is tighter [E^0(Ni$^{I/0}$) − E^0(Ni$^{II/I}$) = −430 mV] (Figure 8C), consistent with electronic increment in the same high-lying $d_{x^2-y^2}$ orbital. The complex is expected to shuttle through a [Ni^I**L**Cl] intermediate, either in a seesaw or a SP geometry, as suggested by structures found for a similar set of Ni(I) PNP halide complexes.[69] Upon reduction to the Ni(0) state, we assume Cl$^-$ dissociation and MeCN association similar to that proposed for Co(0). However, the apparent rate of these follow-up chemical steps [$k_{f,app}$(Ar) = 3.6 × 10^{-1} s^{-1}] is decelerated compared to the Co(0) complex, as witnessed by reversibility of the Ni$^{I/0}$ wave at an elevated scan rate. This point also agrees with the formation of an intermediate closed-shell 18-electron Ni(0) species, more stable than the 17-electron Co(0) congener. The binding of CO_2 at this stage is, however, largely favored, with **Ni$_{Cl}$** displaying the largest cathodic shift $\Delta E_{p,c}^{Ar\rightarrow CO_2}$(M$^{I/0}$) of 130 mV. This shift translates into a follow-up chemical step 4 orders of magnitude faster upon CO_2 addition [$k_{f,app}$(CO_2) = 4.2 × 10^3 s^{-1}], corresponding to the binding of the electrophilic CO_2 substrate. CO_2 activation at a Ni(0) center supported by a neutral PPP ligand was shown to build a pentacoordinated Ni(0) species displaying η^2-CO_2 binding,[70] as crystallographically shown in the famous Aresta complex.[71] Such species are better described as Ni(0) species with minor electron transfer to the bound CO_2. We suggest that **Ni$_{Cl}$** results in a similar [Ni^0**L**(CO_2)] adduct. The reoxidation wave at $E_{p,a}$ = −0.39 V_{Fc} observed at an elevated scan rate (ν = 50 V·s^{-1}) could then relate to the oxidation of a subsequent intermediate, for instance, a [Ni^{II}**L**(CO_2H)]$^+$ hydroxycarbonyl complex formed by the protonation of [Ni^0**L**(CO_2)].

3.4. Comparative Assessment. The groups of Lewis and Fujita have emphasized the relationship between the reduction potential of the metal center and CO_2 coordination on a series of nickel(II) and cobalt(II) cyclam-like complexes.[23,72−75] The CO_2 association equilibrium [K_A(CO_2)] and forward rate [$k_{A,f}$(CO_2)] constants at the +I oxidation state were found to follow a general trend, increasing as the M$^{II/I}$ standard potential becomes more negative.[74] The present series of complexes **Fe$_{MeCN}$**, **Co$_{Cl}$**, and **Ni$_{Cl}$** exhibit reduction potentials sufficiently negative to afford CO_2 coordination. While

https://doi.org/10.1021/acs.inorgchem.1c02909
Inorg. Chem. 2021, 60, 19062−19078

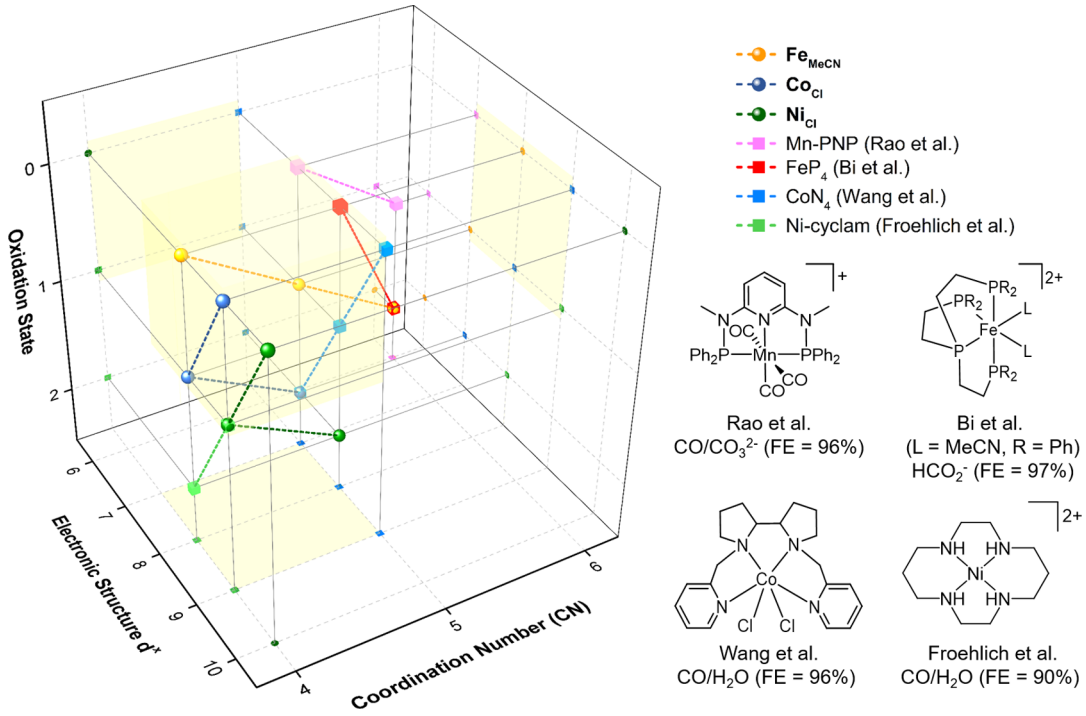

Figure 11. Electronic and geometric properties of $\mathbf{Fe_{MeCN}}$, $\mathbf{Co_{Cl}}$, $\mathbf{Ni_{Cl}}$, and selected eCO_2R catalysts traversing the ET_M mechanism (except Bi et al.) and containing redox-innocent ligand systems.[57,77−79] Metal-centered reduction processes are indicated by dashed lines. The yellow area indicates core electronic/structural properties favoring electrochemical CO_2 activation.

interaction with CO_2 occurs at the +I oxidation state for $\mathbf{Fe_{MeCN}}$, both $\mathbf{Co_{Cl}}$ and $\mathbf{Ni_{Cl}}$ require reduction to a formal M(0) state to proceed to CO_2 activation. This point is in sharp contrast to complexes of the same metals with redox-innocent ligands, where CO_2 coordination already occurs at the formal M(I) state. In particular, $[Ni(cyclam)]^+$, which has a $Ni^{II/I}$ reduction potential $[E^0(Ni^{II/I}) = -1.14\ V_{NHE}$[75] corrected to approximately $-1.77\ V_{Fc}$[76]] close to the $Ni^{I/0}$ one of $\mathbf{Ni_{Cl}}$ $[E^0(Ni^{I/0}) = -1.59\ V_{Fc}]$, exhibits a Ni^I-CO_2 association rate constant $[k_{A,f}(CO_2) = 3.2 \times 10^7\ M^{-1}\cdot s^{-1}$, in aqueous solution[73]] exceeding by several orders of magnitude that found for Ni^0-CO_2 with $\mathbf{Ni_{Cl}}$ $[k_{A,f}(CO_2) = 1.5 \times 10^4\ M^{-1}\cdot s^{-1}$, in an MeCN solution]. We note here that equilibrium and rate constants for CO_2 association at 3d centers in their 0 oxidation state are scarcely reported (we only found reported an order of magnitude of 10^2−$10^3\ s^{-1}$ for the CO_2 association rate constant at the electroreduced 0 state of a $[Co^{II}(PN_3P)(MeCN)_2]^{2+}$ complex).[66] Nevertheless, this difference likely reflects the higher kinetic barrier for CO_2 association at the closed-shell $[Ni^0\mathbf{L}(MeCN)_{n'}]$ complex compared to the open-shell 17-VE $[Ni^I(cyclam)]^+$, underlining the importance of the electronic configuration for binding and activating CO_2.

In agreement with this consideration, the present results indicate that the 17-VE complex $[Co^0\mathbf{L}(MeCN)_{n'}]$ binds CO_2 at faster rates than the 18-VE complex $[Ni^0\mathbf{L}(MeCN)_{n'}]$. A larger degree of CO_2 activation is also suggested by the increase in the $Co^{I/0}$ cathodic peak current upon contact with the substrate. This interpretation is in line with findings for the series of cyclam-like complexes in which Co(I) transfers up to two electrons to the bound CO_2, whereas Ni(I) does not substantially activate the substrate.[75] The electrochemical CO_2 activation by $\mathbf{Co_{Cl}}$ and $\mathbf{Ni_{Cl}}$ within the redox-innocent ligand structure appears to follow the same trend. The two-electron reduction of $\mathbf{Ni_{Cl}}$ at mildly negative potential generates a $[Ni^0\mathbf{L}(\eta^2\text{-}CO_2)]$ complex that cannot be reduced further at the potential of the $Ni^{I/0}$ wave, whereas $[Co^{II}\mathbf{L}(\eta^2\text{-}CO_2)]$ is further reducible at the potential of the $Co^{I/0}$ event and can lead to electrocatalytic turnover.

From an organometallic view, these points relate in the case of $\mathbf{Ni_{Cl}}$ to a coordination of CO_2 at Ni(0) characterized by weak-to-moderate back-bonding according to the Dewar−Chatt−Duncanson model of π-bond coordination. The Ni center remains then in the formal oxidation state 0. By contrast, with $\mathbf{Co_{Cl}}$, the more pronounced electron transfer from the Co(0) metal to the antibonding orbitals of the C═O bond of CO_2 results in a metallaoxirane-type structure. Consequently, the Co(0) center is oxidized to Co(II), and subsequent uptake of another electron can generate cobalt(I) metallacarboxylate as a potential intermediate for catalytic CO_2 reduction.

In Figure 11, we graphically summarize the interplay between the electronic and structural properties of 3d metal complexes based on redox-innocent ligands with their electrochemical CO_2 activation properties. The data comprise the complexes reported in this work ($\mathbf{Fe_{MeCN}}$, $\mathbf{Co_{Cl}}$, and $\mathbf{Ni_{Cl}}$) and literature reports of active CO_2 reduction electrocatalysts. The metal-based redox steps to connect the starting complex and the active species are indicated by the dashed line. All complexes having activity toward CO_2 activation under electrocatalytic conditions show common features within the yellow box indicated in the graph. They are coordinatively unsaturated with coordination number (CN) = 4 or 5, have an open-shell structure of metal electron configuration d^7 to d^9, and are reduced to low oxidation states +I or 0. Consequently, potential electrocatalysts for CO_2 reduction should be designed to meet these three parameters simultaneously upon access of the active species. This combination appears to be a necessary prerequisite but is not sufficient to guarantee

https://doi.org/10.1021/acs.inorgchem.1c02909
Inorg. Chem. 2021, 60, 19062−19078

the electrocatalytic performance. Structural or electronic changes under reaction conditions, viz., by ligand dissociation/exchange or dimerization, must also be considered in the design of CO_2 electroreduction catalysts engaging in the ET_M mechanism. The molecular tools of coordination and organometallic chemistry will be essential to address this challenge.

4. SUMMARY AND CONCLUSION

The series of 3d transition metals M = Mn, Fe, Co, Ni, Cu, and Zn form stable complexes with the redox-innocent pincer ligand **L**. Analysis of the structures of the new ligand and coordination compounds with each metal was achieved by XRD and spectroscopic investigation. We have then put into perspective the structures of the obtained complexes with the requirements for electrochemical CO_2 activation in the ET_M pathway, namely, metal-centered reducibility and CO_2 activation at the reduced states.

The reduction ability at the metal center was found to be primarily dependent on the 3d electron count of the starting complex. The redox innocence of the metal illustrates this point in full-shell d^{10} Cu(I) and Zn(II) species, whereas open-shell complexes $\mathbf{Fe_{MeCN}}$, $\mathbf{Co_{Cl}}$, and $\mathbf{Ni_{Cl}}$ afford metal-centered reduction. This factor alone is still not decisive because the d^6 complex $\mathbf{Mn_{Br}}$ could not be reduced at mild potentials from the initial +I oxidation state likely because of the strong field splitting of the ancillary carbonyl ligands. We emphasize that this behavior strongly deviates from manganese(I) carbonyl complexes that are based on redox-active ligands and are highly competent in CO_2 electroreduction.[80]

Complexes $\mathbf{Fe_{MeCN}}$, $\mathbf{Co_{Cl}}$, and $\mathbf{Ni_{Cl}}$ that reveal distinct metal-centered redox events from M(II) down to M(0) were found to bind CO_2 in their reduced states, as inferred from the electrochemical data. The coordination of CO_2 occurs already at an Fe(I) species in $\mathbf{Fe_{MeCN}}$ but happens at the M(0) state for $\mathbf{Co_{Cl}}$ and $\mathbf{Ni_{Cl}}$. The capability of activating CO_2 by transferring electron(s) to the molecule further depends on the metal. Formed at mildly negative potential, the d^{10} Ni species leads to the association of CO_2 to a putative Aresta-type Ni^0-η^2-CO_2 complex, resulting in only moderate electron transfer to CO_2 through π-back-bonding. This activation mode appears to be insufficient to enable electrocatalytic activity. The d^9 Co(0) intermediate is evolved at 330 mV more negative potential and, after further electron uptake, can lead to a formal cobalt(I) metallacarboxylate complex, which is able to promote turnover.

Our findings, together with the few literature examples of molecular eCO_2R catalysts based on redox-innocent ligands, single out that an unsaturated coordination sphere (CN = 4 or 5) and a d^7-to-d^9 configuration at the reduced state (+I or 0) are characteristic for 3d metal complexes enabling an ET_M mechanism. The design of complexes that purposely meet these three characteristics simultaneously provides a promising strategy for catalyst development. However, dynamic structural and electronic changes under electrochemical conditions must also be controlled to ensure the primary operation of the metal centers in the desired catalytic manifold. This challenge may be approached by optimizing the molecular framework of a privileged coordination environment through systematic ligand variation, as is well-established for numerous examples in organometallic catalysis. Along these lines, investigations are underway in our laboratory to benchmark the metal-centered properties and structural variations of the ligand lead structure against the electrocatalytic performance.

5. EXPERIMENTAL SECTION

5.1. General Considerations. *5.1.1. Synthesis and Structural Analysis.* All synthetic manipulations were performed under an Ar atmosphere either in an MBraun UNILAB Plus glovebox or by use of standard Schlenk techniques in oven-dried glassware, ensuring rigorously inert conditions. Organic solvents were dried and degassed by passage over an MBraun SPS-7 solvent purification system, handled under an Ar atmosphere, and stored over molecular sieves. Commercially available chemicals were purchased from Merck, Carl Roth, TCI, or abcr and used without further purification if not otherwise stated. NMR solvents were degassed by three freeze–pump–thaw cycles and dried over molecular sieves. Aniline was dried over molecular sieves and degassed by purging with Ar. Tetrabutylammonium hexafluorophosphate was dried and degassed at 80 °C under vacuum for 12 h.

NMR spectra were recorded on a Bruker AVANCE NEO 400 MHz or a Bruker AVANCE III HD 500 MHz NMR spectrometer with a Bruker Prodigy probe at the indicated temperature. Chemical shifts (δ) are given in parts per million related to tetramethylsilane (TMS) and the coupling constants (J) in hertz. The solvent residual signal was used as a reference, and the chemical shift was converted to the TMS scale (CD_2Cl_2, δ_H = 5.32 ppm and δ_C = 53.84 ppm; CD_3CN, δ_H = 1.94 ppm and δ_C = 1.32 ppm).[81] First-order spin multiplicities are abbreviated as singlet (s), doublet (d), triplet (t), and quadruplet (q). Couplings of higher-order or overlapped signals are denoted as m (multiplet) and broadened signals as br. Indications of the positions of the H and C atoms in aromatic rings are given as ortho (o), meta (m), para (p), and quaternary (q).

HRMS was recorded on a Thermo Scientific Q Exactive Plus Hybrid Quadrupole-Orbitrap mass spectrometer. UV/vis measurements were conducted on an Agilent Technologies Cary 8454 UV/vis spectroscopy system.

Elemental analysis (C, H, and N) was performed on an Elementar UNICUBE fitted with a thermal conductivity detector.

Single crystals of compounds CCDC 2109420–2109432 were selected under a microscope in polarized light with an applied nitrogen cryostream at approximately −40 °C and covered with polyfluorinated polyether. The crystals were picked up with nylon loops and rapidly mounted in the nitrogen cold gas stream of the diffractometer at 100 K to prevent solvent loss. A Bruker D8 Venture diffractometer equipped with a IμS3 Diamond source, INCOATEC Helios mirror optics (Mo Kα radiation; λ = 0.71073 Å), and a Photon III detector were used for data collection. Data were processed using the Bruker *APEX 3* software suite. The final cell constants are based on refinement of the *XYZ* centroids of several thousand reflections above 20 $\sigma(I)$. Structures were solved and refined using the embedded Bruker *SHELXTL* software package. All non-H atoms were anisotropically refined, and H atoms were placed at calculated positions and refined as riding atoms with isotropic displacement parameters.

The magnetic susceptibility data were measured with powder samples in the temperature range 2–270 K by using a SQUID susceptometer with a field of 1.0 T (MPMS-3, Quantum Design, calibrated with a standard palladium reference sample; error <2%). Multiple-field variable-temperature magnetization measurements were done at 1, 4, and 7 T in the range of 2–260 K with the magnetization equidistantly sampled on a $1/T$ temperature scale. Sample holders of quartz with O-ring sealing were used, and the SQUID response curves (raw data) have been corrected for holder and solvent contributions by subtracting the corresponding response curves obtained from separate measurements without sample material. The experimental magnetization data obtained from an independent simulation of the corrected SQUID response curves were corrected for underlying diamagnetism by use of tabulated Pascal's constants, as well as for temperature-independent paramagnetism. Handling and simulation of the SQUID raw data as well as spin-Hamiltonian simulation of the susceptibility and magnetization data were done with our own package *julX.SL* for exchange-coupled systems (available from E.B. by emailing ebill@gwdg.de).

https://doi.org/10.1021/acs.inorgchem.1c02909
Inorg. Chem. 2021, 60, 19062–19078

^{57}Fe Mössbauer spectra were recorded with nonenriched powder samples on a conventional spectrometer with alternating constant acceleration of the γ source (^{57}Co/Rh, 1.8 GBq). The source was kept at rt, and the sample temperature was maintained constant in an Oxford Instruments Variox cryostat. The raw data (512 channels) were folded to merge the two recorded mirror images of the spectra, which also eliminates the parabolic background. The minimum experimental linewidth was 0.24 mm·s^{-1} (full width at half-maximum). Isomer shifts are quoted relative to iron metal at 300 K because the spectrometer was calibrated by recording the Mössbauer spectrum of a 12-μm-thick foil of α-Fe at rt, with the center of the six-line pattern being taken as zero velocity. The *mf.SL* package (version 2.2 by E.B.) was used to simulate the spectra with Lorentzian doublets, or doublet Voigt profiles, with least-squares parameter optimization.

X-band EPR derivative spectra were recorded with frozen-solution samples (ca. 1 mM) on a Bruker ELEXSYS E500 spectrometer equipped with the Bruker dual-mode cavity (ER4116DM) and a helium-flow cryostat (Oxford Instruments ESR 910). The microwave unit was the Bruker high-sensitivity Super-X bridge (ER-049X) with an integrated microwave frequency counter. The magnetic field controller (ER032T) was externally calibrated with a Bruker NMR field probe (ER035M). The spectra were simulated with the program *esimX.SL* (by E.B.) for calculation of the powder spectra with effective g values and first-order hyperfine splitting and anisotropic linewidths (Gaussian line shapes were used).

5.1.2. Electrochemical Analysis. Electrochemical investigations were performed on a BioLogic VSP-300 potentiostat equipped with an analogue ramp generator for high potential scan rate analysis in a standard three-electrode setup with a glassy carbon working electrode (WE), a platinum wire counter electrode (CE), and a Ag/$AgNO_3$ (10 mM $AgNO_3$ in a solution of 0.1 M ^{n}Bu$_4$NPF$_6$ in the electrochemical solvent) reference electrode (RE). The WE was polished over a polishing pad using an alumina suspension before rinsing with ultrapure water from a Milli-Q Advantage A10 water purification system and then with ethanol. RE and CE were rinsed with ultrapure water and ethanol. Lastly, each electrode was dried under a stream of argon before insertion into the cell. The ohmic drop of the electrochemical cell was estimated and compensated for (85%) by the *iR* compensation loop embedded in the potentiostat.

In general, a 1 mM solution of the analyte in a dry and degassed solution of 0.1 M ^{n}Bu$_4$NPF$_6$ in the electrochemical solvent was prepared for analysis. Prior to the addition of the analyte, the electrolyte solution was purged by bubbling a solvent-saturated argon flow through silicon tubing under vigorous stirring. The scanned potential window was adjusted according to the visible redox waves, and parameter variations are indicated in the respective measurements. Cyclic voltammograms were typically recorded at a scan rate of 0.1 V·s^{-1}. For experiments under CO_2, the electrolyte solution was sparged with a solvent-saturated CO_2 flow for 20 min before measurements were performed.

At the end of a measurement row, ferrocene (1 mM) was added as the internal potential reference.

5.2. Synthesis. *5.2.1. Ligand. N^2,N^6-Diphenylpyridine-2,6-diamine.* The synthesis was performed according to a modified procedure of Wagaw and Buchwald.[40] 2,6-Dibromopyridine (0.4978 g, 2.00 mmol, 1.00 equiv), aniline (0.3725 g, 0.37 mL, 4.00 mmol, 2.00 equiv), tris(dibenzylideneacetone)dipalladium [$Pd_2(dba)_3$; 0.0366 g, 0.0400 mmol, 0.0200 equiv], 1,3-bis(diphenylphosphino)-propane (dppp; 0.0330 g, 0.0800 mmol, 0.0400 equiv), and potassium *tert*-butoxide (0.6284 g, 5.60 mmol, 2.80 equiv) were placed in a Schlenk tube in the glovebox, and toluene was added (15 mL). The suspension was stirred at 100 °C for 18 h and cooled to rt before dichloromethane (DCM; 10 mL) was added. The organic phase was washed with brine (20 mL), the resulting aqueous phase was extracted with DCM (3 × 10 mL), and the combined organic layers were dried over anhydrous magnesium sulfate. After removal of the organic solvents *in vacuo*, the crude product was purified by column chromatography on silica using a mixture of pentane and ethyl acetate (85:15). The desired product was received as an orange solid (0.397 g, 1.52 mmol, 76%). The obtained analytical data are consistent with those previously reported in the literature.[40]

N^2,N^6-Bis(diphenylphosphanyl)-N^2,N^6-diphenylpyridine-2,6-diamine (L). *n*-Butyllithium (2.5 M in hexanes, 4.0 mL, 10.0 mmol, 2.0 equiv) was added dropwise to an orange solution of N^2,N^6-diphenylpyridine-2,6-diamine (1.3067 g, 5.00 mmol, 1.00 equiv) in THF (35 mL) at −78 °C. The solution was allowed to warm up to rt and stirred for 1 h before cooling down again to 0 °C and dropwise addition of chlorodiphenylphosphine (1.84 mL, 10.0 mmol, 2.0 equiv). The solution was allowed to warm up to rt and stirred at rt for 1 h, then at 65 °C for 18 h. After cooling to rt, the solvents were removed *in vacuo*, and the brown residue was washed with MeOH (4 × 10 mL), diethyl ether (Et_2O; 3 × 5 mL), and pentane (3 × 5 mL). Removal of the residual solvents *in vacuo* yielded the desired product **L** as a white solid (2.1 g, 3.3 mmol, 67%). Crystals suitable for XRD were obtained from a concentrated THF/pentane (3:1) solution at −35 °C. ^{1}H NMR (500 MHz, CD_2Cl_2, 296 K): δ_H 7.28−7.16 (m, 12H, PPhH_m + PPhH_p), 7.15−7.07 (m, 9H, PPhH_o + PyH_p), 7.02−6.95 (m, 6H, NPhH_m + NPhH_p), 6.82−6.76 (m, 4H, NPhH_o), 5.81 (d, 2H, J = 8.0, PyH_m). ^{13}C{^{1}H} NMR (126 MHz, CD_2Cl_2, 296 K): δ_C 160.3−159.7 (m, PyC_q), 143.1−142.8 (m, NPhC_q), 139.5−138.8 (m, PPhC_q), 138.6 (PyC_p), 133.9−133.3 (m, PPhC_m), 130.9 (NPhC_o), 129.1 (NPhC_m), 128.8 (PPhC_p), 128.0 (t, J = 2.9, PPhC_o), 126.4 (NPhC_p), 101.5 (PyC_m). ^{31}P{^{1}H} NMR (202 MHz, CD_2Cl_2, 296 K): δ_P 52.8. HRMS (ESI$^+$). Calcd for $C_{41}H_{33}N_3P_2$ + H$^+$: m/z 630.22225. Found: m/z 630.22213. Elem anal. Calcd for $C_{41}H_{33}N_3P_2$: C, 78.21; H, 5.28; N, 6.67. Found: C, 78.36; H, 5.15; N, 6.64.

5.2.2. Complexes. **General procedure: L** (0.0315 g, 0.0500 mmol, 1.00 equiv) and the respective metal precursor (0.0500 mmol, 1.00 equiv) were placed in a Schlenk tube in a glovebox, and the respective solvent (2 mL) was added. The resulting solution was stirred at the indicated temperature for 16 h before removal of the solvent *in vacuo*. Purification steps and deviations from the general procedure are explicated below for each complex.

[Mn**L**(CO)$_2$Br] (**Mn$_{Br}$**): Reaction conditions: Mn(CO)$_5$Br, toluene, 110 °C. The desired product **Mn$_{Br}$** was obtained as a yellow solid after the residue was washed with DCM (2 mL) and pentane (3 × 2 mL) prior to removal of the solvent *in vacuo*. Yield: 30.8 mg, 0.0375 mmol, 75%. In concentrated solutions of DCM and under exposure to light, a change of color to brown, possibly upon CO loss and dimerization, was observed. Crystals suitable for XRD were obtained from the vapor diffusion of pentane into a concentrated DCM solution under exclusion of light. ^{1}H NMR (500 MHz, CD_2Cl_2, 296 K): δ_H 7.77 (dd, 4H, J = 5.8 and 5.1), 7.47−7.36 (m, 10H), 7.36−7.27 (m, 8H), 7.26−7.13 (m, 7H, PyH_p), 6.81 (d, 2H, J = 8.0, NPhH_o), 5.79 (d, 2H, J = 8.2, PyH_m). ^{13}C{^{1}H} NMR (126 MHz, CD_2Cl_2, 296 K): δ_C 178.0 (CO), 164.1 (t, J = 12.9, PyC_q), 141.3 (NPhC_q), 139.9 (t, J = 23.4, PPhC_q), 139.1 (PyC_p), 137.5 (t, J = 6.3), 132.5, 131.8, 131.7 (t, J = 5.7), 131.5, 130.6, 130.3, 130.2, 130.1, 128.8, 128.2 (t, J = 4.6), 127.4 (t, J = 5.0), 102.9 (PyC_m). ^{31}P{^{1}H} NMR (202 MHz, CD_2Cl_2, 296 K): δ_P 138.9. HRMS (ESI$^+$). Calcd for $C_{43}H_{33}BrMnN_3O_2P_2^+$: m/z 819.06064. Found: m/z 819.06076. Elem anal. Calcd for $C_{43}H_{33}BrMnN_3O_2P_2$·0.1 C_7H_8: C, 63.26; H, 4.11; N, 5.06. Found: C, 63.66; H, 4.44; N, 4.99.

[Fe**L**Cl$_2$] (**Fe$_{Cl}$**): Reaction conditions: $FeCl_2$, DCM, rt. The crude product was purified by precipitation from a DCM solution with pentane. **Fe$_{Cl}$** was obtained as a yellow solid after the precipitate was washed with pentane (3 × 2 mL) and the solvent was removed *in vacuo*. Yield: 30.8 mg, 0.0476 mmol, 95%. Crystals suitable for XRD were obtained from a concentrated DCM/pentane (3:1) solution at −35 °C. ^{1}H NMR (500 MHz, CD_2Cl_2, 296 K): δ_H 57.14 (s br, 2H, PyH_m), 14.38 (s br, 8H, PPhH_m), 8.61 (s br, 4H, NPhH_m), 3.52 (s br, 4H, NPhH_o), 3.13 (s br, 2H, NPhH_p), −4.92 (s br, 8H, PPhH_o), −5.45 (s br, 4H, PPhH_p), −11.61 (s br, 1H, PyH_p). ^{13}C{^{1}H} NMR (126 MHz, CD_2Cl_2, 296 K): δ_C 282.7, 258.5, 199.5, 155.0, 152.1, 116.9, 108.6. HRMS (ESI$^+$). Calcd for $C_{41}H_{33}ClFeN_3P_2^+$: m/z 720.11821. Found: m/z 720.11849. Elem anal. Calcd for $C_{41}H_{33}Cl_2FeN_3P_2$: C, 65.10; H, 4.40; N, 5.56. Found: C, 65.31; H, 4.79; N, 5.28.

https://doi.org/10.1021/acs.inorgchem.1c02909
Inorg. Chem. 2021, 60, 19062−19078

Crystals of [**FeL**(MeCN)$_3$](**Cl$_3$FeOFeCl$_3$**) were obtained from a concentrated MeCN/Et$_2$O (3:1) solution of **Fe$_{Cl}$** at −30 °C under air.

[Fe**L**(MeCN)$_3$](OTf)$_2$ (**Fe$_{MeCN}$**): Reaction conditions: Fe(OTf)$_2$, MeCN, rt. The desired product **Fe$_{MeCN}$** was obtained as an orange solid after washing with Et$_2$O (2 mL) and pentane (3 × 2 mL) prior to the removal of the solvent *in vacuo*. Yield: 48.9 mg, 0.0442 mmol, 88%. Crystals suitable for XRD were obtained from a concentrated MeCN/Et$_2$O (3:1) solution at −35 °C. ^{1}H NMR (500 MHz, CD$_2$Cl$_2$, 298 K): δ_H 7.75−7.59 (m, 12H, PPhH_o + PPhH_p), 7.60−7.50 (m, 8H, PPhH_m), 7.48−7.37 (m, 6H, NPhH_m + NPhH_p), 7.34 (t, 1H, J = 8.2, PyH_p), 7.10 (d, 4H, J = 7.4, NPhH_o), 5.99 (d, 2H, J = 8.2, PyH_m), 2.43 (s, 3H, CH_3CN$_{eq}$), 1.73 (s, 6H, CH_3CN$_{ax}$). ^{13}C{^{1}H} NMR (126 MHz, CD$_2$Cl$_2$, 296 K): δ_C 166.0 (t, J = 11.1, PyC$_q$), 141.8 (PyC$_p$), 139.2 (t, J = 2.7, NPhC$_q$), 138.7 (CH$_3$CN$_{eq}$), 138.1 (CH$_3$CN$_{ax}$), 134.1 (t, J = 6.3, PPhC$_o$), 132.9 (PPhC$_p$), 131.1 (NPhC$_m$), 130.5 (NPhC$_o$), 129.9 (NPhC$_p$), 129.7 (t, J = 2.7, PPhC$_m$), 129.5 (PPhC$_q$), 129.3, 104.5 (t, J = 2.3, PyC$_m$), 5.4 (CH$_3$CN$_{eq}$), 4.7 (CH$_3$CN$_{ax}$). ^{31}P{^{1}H} NMR (202 MHz, CD$_2$Cl$_2$, 296 K): δ_P 129.2. HRMS (ESI$^+$). Calcd for $C_{43}H_{36}FeN_4P_2^{2+}$: m/z 363.08768. Found: m/z 363.08752. Elem anal. Calcd for $C_{49}H_{42}F_6FeN_6O_6P_2S_2$·0.25 $C_4H_{10}O$: C, 53.37; H, 3.99; N, 7.47. Found: C, 53.04; H, 4.33; N, 7.12.

[Co**L**Cl$_2$] (**Co$_{Cl}$**): Reaction conditions: CoCl$_2$, THF, rt. The crude product was purified by precipitation with pentane from a THF solution. **Co$_{Cl}$** was obtained as a dark-red solid after the precipitate was washed with pentane (3 × 2 mL) and the solvent was removed *in vacuo*. Yield: 34.0 mg, 0.0448 mmol, 90%. Crystals suitable for XRD were obtained from the vapor diffusion of pentane into a concentrated THF solution or from a concentrated MeCN/Et$_2$O (3:1) solution at −35 °C.

^{1}H NMR (400 MHz, CD$_2$Cl$_2$, 296 K): δ_H 10.65 (br s, 1H), 9.40 (br s, 4H), 8.61 (br s, 4H), 8.34−7.07 (m, 16H), 5.97 (br s, 8H). HRMS (ESI$^+$). Calcd for $C_{41}H_{33}Cl_2CoN_3P_2^+$: m/z 758.08533. Found: m/z 758.08561. Elem anal. Calcd for $C_{41}H_{33}Cl_2CoN_3P_2$: C, 64.84; H, 4.38; N, 5.53. Found: C, 64.56; H, 4.27; N, 5.48.

[Ni**L**Cl$_2$] (**Ni$_{Cl}$**): Reaction conditions: NiCl$_2$·DME, DCM, rt. The desired product **Ni$_{Cl}$** was obtained as a red solid after the crude product was precipitated from a solution of DCM with pentane, followed by washing of the residue with pentane (3 × 2 mL) and removal of the solvent *in vacuo*. Yield: 34.2 mg, 0.0450 mmol, 90%. Crystals suitable for XRD were obtained from a concentrated DCM/pentane (3:1) solution or a concentrated MeCN/Et$_2$O (3:1) solution at −35 °C.

^{1}H NMR (500 MHz, CD$_2$Cl$_2$, 296 K): δ_H 7.90 (d, 8H, J = 6.3, PPhH_o), 7.63 (t, 4H, J = 7.4, PPhH_p), 7.48 (t, 8H, J = 7.5, PPhH_m), 7.41−7.31 (m, 3H, NPhH_p + PyH_p), 7.27 (t, 4H, J = 7.5, NPhH_m), 6.92 (d, 4H, J = 7.6, NPhH_o), 5.73 (d, 2H, J = 8.2, PyH_m). ^{13}C{^{1}H} NMR (126 MHz, CD$_2$Cl$_2$, 296 K): δ_C 163.8 (PyC$_q$), 142.8 (PyC$_p$), 137.9 (NPhC$_q$), 134.7 (PPhC$_o$), 133.1 (PPhC$_p$), 130.6 (NPhC$_o$), 130.1 (NPhC$_m$), 129.6 (NPhC$_p$), 129.2 (PPhC$_m$), 126.2 (t, J = 23.7, PPhC$_q$), 103.4 (PyC$_m$). ^{31}P{^{1}H} NMR (202 MHz, CD$_2$Cl$_2$, 296 K): δ_P 85.0. HRMS (ESI$^+$). Calcd for $[C_{41}H_{33}Cl_2N_3NiP_2 - Cl]^+$: m/z 722.11862. Found: m/z 722.11871. Elem anal. Calcd for $C_{41}H_{33}Cl_2N_3NiP_2$·0.2 CH_2Cl_2: C, 63.75; H, 4.34; N, 5.41. Found: C, 63.55; H, 4.57; N, 5.43.

[Cu**L**Cl] (**Cu$_{Cl}$**): Reaction conditions: CuCl, THF, rt. The desired product **Cu$_{Cl}$** was obtained as a light-yellow solid after precipitation from a solution in DCM with pentane and washing of the residue with pentane (3 × 2 mL) before removal of the residual solvent *in vacuo*. Yield: 23.9 mg, 0.0327 mmol, 66%. Crystals suitable for XRD were obtained from a concentrated DCM/pentane (3:1) solution at −35 °C.

^{1}H NMR (500 MHz, CD$_2$Cl$_2$, 296 K): δ_H 7.50 (dd, 8H, J = 5.8 and 5.3, PPhH_o), 7.31 (t, 4H, J = 7.4, PPhH_p), 7.24 (t, 1H, J = 8.0, PyH_p), 7.17 (t, 8H, J = 7.6, PPhH_m), 7.15−7.08 (m, 6H, NPhH_m + NPhH_p), 6.93−6.83 (m, 4H, NPhH_o), 5.68 (d, 2H, J = 8.0, PyH_m). ^{13}C{^{1}H} NMR (126 MHz, CD$_2$Cl$_2$, 296 K): δ_C 157.8 (t, J = 9.4, PyC$_q$), 141.6 (PyC$_p$), 140.1 (t, J = 3.0, NPhC$_q$), 133.6 (PPhC$_o$), 132.9 (t, J = 11.4, PPhC$_q$), 130.9 (NPhC$_o$), 130.4 (PPhC$_p$), 129.7 (NPhC$_m$), 128.5 (t, J = 4.4, PPhC$_m$), 127.9 (NPhC$_p$), 101.1 (PyC$_m$). ^{31}P{^{1}H} NMR (202 MHz, CD$_2$Cl$_2$, 296 K): δ_P 39.9. HRMS (ESI$^+$). Calcd for $C_{41}H_{33}ClCuN_3P_2^+$: m/z 727.11288. Found: m/z 727.11272. Elem anal. Calcd for $C_{41}H_{33}ClCuN_3P_2$·0.05 CH_2Cl_2: C, 67.27; H, 4.55; N, 5.73. Found: C, 67.02; H, 4.75; N, 5.48.

[Cu**L**I] (**Cu$_I$**): Reaction conditions: CuI, THF, 65 °C. The desired product **Cu$_I$** was obtained as a white solid by precipitating the crude product from a DCM solution with pentane, washing the residue with pentane (3 × 2 mL), and removing the solvent *in vacuo*. Yield: 21.3 mg, 0.0260 mmol, 52%. Crystals suitable for XRD were obtained from a concentrated THF solution at −35 °C.

^{1}H NMR (500 MHz, CD$_2$Cl$_2$, 296 K): δ_H 7.62−7.41 (m, 8H, PPhH_o), 7.36−7.23 (m, 5H, PPhH_p + PyH_p), 7.21−7.06 (m, 14H, PPhH_m + NPhH_m + NPhH_p), 7.01−6.89 (m, 4H, NPhH_o), 5.67 (d, 2H, J = 8.0, PyH_m). ^{13}C{^{1}H} NMR (126 MHz, CD$_2$Cl$_2$, 296 K): δ_C 157.7 (t, J = 9.2, PyC$_q$), 141.6 (PyC$_p$), 140.0 (t, J = 2.7, NPhC$_q$), 133.7 (PPhC$_o$), 132.6 (t, J = 11.7, PPhC$_q$), 130.9 (NPhC$_o$), 130.4 (PPhC$_p$), 129.7 (NPhC$_m$), 128.4 (t, J = 4.4, PPhC$_m$), 127.9 (NPhC$_p$), 101.2 (PyC$_m$). ^{31}P{^{1}H} NMR (202 MHz, CD$_2$Cl$_2$, 296 K): δ_P 40.0. HRMS (ESI$^+$). Calcd for $C_{41}H_{33}CuIN_3P_2^+$: m/z 819.04849. Found: m/z 819.04742. Elem anal. Calcd for $C_{41}H_{33}CuIN_3P_2$: C, 60.05; H, 4.06; N, 5.12. Found: C, 59.82; H, 4.18; N, 5.06.

[Zn**L**Cl$_2$] (**Zn$_{Cl}$**): Reaction conditions: ZnCl$_2$, THF, rt. The desired product **Zn$_{Cl}$** was obtained as a white solid by precipitating the crude product from a solution of DCM with pentane, followed by washing of the residue with pentane (3 × 2 mL) and removal of the solvent *in vacuo*. Yield: 33.3 mg, 0.0434 mmol, 87%. Crystals suitable for XRD were obtained from a concentrated THF/pentane (3:1) solution at −35 °C.

^{1}H NMR (500 MHz, CD$_2$Cl$_2$, 296 K): δ_H 7.46−7.39 (m, 8H, PPhH_o), 7.34−7.28 (m, 5H, PPhH_p + PyH_p), 7.24−7.08 (m, 14H, PPhH_m + NPhH_m + NPhH_p), 7.03−6.90 (m, 4H, NPhH_o), 5.85 (d, 2H, J = 8.1, PyH_m). ^{13}C{^{1}H} NMR (126 MHz, CD$_2$Cl$_2$, 296 K): δ_C 157.4 (t, J = 7.3, PyC$_q$), 141.4 (PyC$_p$), 138.7 (NPhC$_q$), 133.8 (PPhC$_o$), 131.6 (PPhC$_p$), 131.2 (NPhC$_o$), 129.9 (NPhC$_m$), 128.9 (t, J = 4.9, PPhC$_m$), 128.4 (NPhC$_p$), 101.8 (PyC$_m$). ^{31}P{^{1}H} NMR (202 MHz, CD$_2$Cl$_2$, 296 K): δ_P 30.9. HRMS (ESI$^+$). Calcd for $[C_{41}H_{33}N_3P_2ZnCl_2 - Cl]^+$: m/z 728.11242. Found: m/z 728.11180. Elem anal. Calcd for $C_{41}H_{33}Cl_2N_3P_2Zn$·0.25 CH_2Cl_2: C, 62.94; H, 4.29; N, 5.34. Found: C, 62.67; H, 4.30; N, 5.33.

[Zn**L**(OTf)$_2$] (**Zn$_{OTf}$**): Reaction conditions: Zn(OTf)$_2$, MeCN, 80 °C. The desired product **Zn$_{OTf}$** was obtained as a white solid by precipitating the crude product from a solution of DCM with pentane, washing the residue with pentane (3 × 2 mL), and removing the solvent *in vacuo*. Yield: 47.4 mg, 0.0477 mmol, 95%. Crystals suitable for XRD were obtained from a concentrated THF solution at −35 °C.

^{1}H NMR (500 MHz, CD$_2$Cl$_2$, 296 K): δ_H 7.45−7.36 (m, 13H, PPhH_o + PPhH_p + PyH_p), 7.25 (t, 8H, J = 7.7, PPhH_m), 7.22−7.14 (m, 6H, NPhH_m + NPhH_p), 7.03 (s br, 4H, NPhH_o), 5.94 (d, 2H, J = 8.2, PyH_m). ^{13}C{^{1}H} NMR (126 MHz, CD$_2$Cl$_2$, 296 K): δ_C 157.5 (t, J = 6.8, PyC$_q$), 143.2 (PyC$_p$), 138.0 (t, J = 2.4, NPhC$_q$), 133.9 (br, PPhC$_q$), 132.5 (PPhC$_o$), 130.7 (br, NPhC$_o$), 130.3 (NPhC$_m$), 129.2 (t, J = 5.2, PPhC$_m$), 129.0 (PPhC$_p$), 126.0 (NPhC$_p$), 120.1 (q, CF$_3$), 102.9 (PyC$_m$). ^{31}P{^{1}H} NMR (202 MHz, CD$_2$Cl$_2$, 296 K): δ_P 28.8. HRMS (ESI$^+$). Calcd for $[C_{43}H_{33}F_6N_3O_6P_2S_2Zn - CF_3SO_3]^+$: m/z 842.09559. Found: m/z 842.09613. Elem anal. Calcd for $C_{43}H_{33}F_6N_3O_6P_2S_2Zn$: C, 52.00; H, 3.35; N, 4.23. Found: C, 52.26; H, 3.68; N, 4.32.

■ ASSOCIATED CONTENT

Supporting Information

The Supporting Information is available free of charge at https://pubs.acs.org/doi/10.1021/acs.inorgchem.1c02909.

^{1}H, ^{13}C and ^{31}P NMR, UV/vis, EPR, and Mössbauer spectra, magnetic susceptibility measurements, additional XRD molecular structures and XRD data, and additional CV and electrochemical analysis (PDF)

Accession Codes

CCDC 2109420−2109432 contain the supplementary crystallographic data for this paper. These data can be obtained

https://doi.org/10.1021/acs.inorgchem.1c02909
Inorg. Chem. 2021, 60, 19062−19078

free of charge via www.ccdc.cam.ac.uk/data_request/cif, or by emailing data_request@ccdc.cam.ac.uk, or by contacting The Cambridge Crystallographic Data Centre, 12 Union Road, Cambridge CB2 1EZ, UK; fax: +44 1223 336033.

AUTHOR INFORMATION

Corresponding Authors

Nicolas Kaeffer − *Max Planck Institute for Chemical Energy Conversion, 45470 Mülheim an der Ruhr, Germany;* orcid.org/0000-0002-3166-8551; Email: nicolas.kaeffer@cec.mpg.de

Walter Leitner − *Max Planck Institute for Chemical Energy Conversion, 45470 Mülheim an der Ruhr, Germany; Institut für Technische und Makromolekulare Chemie, RWTH Aachen University, 52074 Aachen, Germany;* orcid.org/0000-0001-6100-9656; Email: walter.leitner@cec.mpg.de

Authors

Niklas W. Kinzel − *Max Planck Institute for Chemical Energy Conversion, 45470 Mülheim an der Ruhr, Germany; Institut für Technische und Makromolekulare Chemie, RWTH Aachen University, 52074 Aachen, Germany*

Derya Demirbas − *Max-Planck-Institut für Kohlenforschung, 45470 Mülheim an der Ruhr, Germany*

Eckhard Bill − *Max Planck Institute for Chemical Energy Conversion, 45470 Mülheim an der Ruhr, Germany;* orcid.org/0000-0001-9138-3964

Thomas Weyhermüller − *Max Planck Institute for Chemical Energy Conversion, 45470 Mülheim an der Ruhr, Germany;* orcid.org/0000-0002-0399-7999

Christophe Werlé − *Max Planck Institute for Chemical Energy Conversion, 45470 Mülheim an der Ruhr, Germany; Ruhr University Bochum, 44801 Bochum, Germany;* orcid.org/0000-0002-2174-2148

Complete contact information is available at: https://pubs.acs.org/10.1021/acs.inorgchem.1c02909

Funding

Open access funded by Max Planck Society.

Notes

The authors declare no competing financial interest.

ACKNOWLEDGMENTS

We gratefully acknowledge basic support from the Max Planck Society, the RWTH Aachen University, and the Ruhr University Bochum. The work was supported by the Deutsche Forschungsgemeinschaft (German Research Foundation) under Germany's Excellence Strategy—Exzellenzcluster 2186 "The Fuel Science Center" (ID: 390919832) funded by the German Federal Ministry of Education and Research. The authors thank Julia Zerbe and Lukas Föbinger for their help with synthesis of the complexes and Kira Ehmann for proof reading the manuscript.

REFERENCES

(1) Zimmerman, J. B.; Anastas, P. T.; Erythropel, H. C.; Leitner, W. Designing for a green chemistry future. *Science* **2020**, *367* (6476), 397−400.

(2) Aresta, M.; Dibenedetto, A. Utilisation of CO2 as a chemical feedstock: opportunities and challenges. *Dalton Trans.* **2007**, *28*, 2975−2992.

(3) Artz, J.; Mueller, T. E.; Thenert, K.; Kleinekorte, J.; Meys, R.; Sternberg, A.; Bardow, A.; Leitner, W. Sustainable Conversion of Carbon Dioxide: An Integrated Review of Catalysis and Life Cycle Assessment. *Chem. Rev.* **2018**, *118* (2), 434−504.

(4) Inoue, S.; Koinuma, H.; Tsuruta, T. Copolymerization of carbon dioxide and epoxide. *J. Polym. Sci., Part B: Polym. Lett.* **1969**, *7* (4), 287−292.

(5) Nakano, R.; Ito, S.; Nozaki, K. Copolymerization of carbon dioxide and butadiene via a lactone intermediate. *Nat. Chem.* **2014**, *6* (4), 325−331.

(6) Tamura, M.; Ito, K.; Honda, M.; Nakagawa, Y.; Sugimoto, H.; Tomishige, K. Direct Copolymerization of CO_2 and Diols. *Sci. Rep.* **2016**, *6* (1), 24038.

(7) Klankermayer, J.; Leitner, W. Love at second sight for CO2 and H2 in organic synthesis. *Science* **2015**, *350* (6261), 629−630.

(8) Wesselbaum, S.; Moha, V.; Meuresch, M.; Brosinski, S.; Thenert, K. M.; Kothe, J.; Stein, T. v.; Englert, U.; Hölscher, M.; Klankermayer, J.; Leitner, W. Hydrogenation of carbon dioxide to methanol using a homogeneous ruthenium−Triphos catalyst: from mechanistic investigations to multiphase catalysis. *Chem. Sci.* **2015**, *6* (1), 693−704.

(9) Klankermayer, J.; Wesselbaum, S.; Beydoun, K.; Leitner, W. Selective Catalytic Synthesis Using the Combination of Carbon Dioxide and Hydrogen: Catalytic Chess at the Interface of Energy and Chemistry. *Angew. Chem., Int. Ed.* **2016**, *55* (26), 7296−7343.

(10) Francke, R.; Schille, B.; Roemelt, M. Homogeneously Catalyzed Electroreduction of Carbon Dioxide-Methods, Mechanisms, and Catalysts. *Chem. Rev.* **2018**, *118* (9), 4631−4701.

(11) Chen, L.; Chen, G.; Leung, C.-F.; Cometto, C.; Robert, M.; Lau, T.-C. Molecular quaterpyridine-based metal complexes for small molecule activation: water splitting and CO2 reduction. *Chem. Soc. Rev.* **2020**, *49* (20), 7271−7283.

(12) Yan, M.; Kawamata, Y.; Baran, P. S. Synthetic Organic Electrochemical Methods Since 2000: On the Verge of a Renaissance. *Chem. Rev.* **2017**, *117* (21), 13230−13319.

(13) Mohle, S.; Zirbes, M.; Rodrigo, E.; Gieshoff, T.; Wiebe, A.; Waldvogel, S. R. Modern Electrochemical Aspects for the Synthesis of Value-Added Organic Products. *Angew. Chem., Int. Ed.* **2018**, *57* (21), 6018−6041.

(14) Nielsen, D. U.; Hu, X.-M.; Daasbjerg, K.; Skrydstrup, T. Chemically and electrochemically catalysed conversion of CO2 to CO with follow-up utilization to value-added chemicals. *Nat. Catal.* **2018**, *1* (4), 244−254.

(15) Ponsard, L.; Nicolas, E.; Tran, N. H.; Lamaison, S.; Wakerley, D.; Cantat, T.; Fontecave, M. Coupling Electrocatalytic CO2 Reduction with Thermocatalysis Enables the Formation of a Lactone Monomer. *ChemSusChem* **2021**, *14* (10), 2198−2204.

(16) Bullock, R. M.; Chen, J. G.; Gagliardi, L.; Chirik, P. J.; Farha, O. K.; Hendon, C. H.; Jones, C. W.; Keith, J. A.; Klosin, J.; Minteer, S. D.; Morris, R. H.; Radosevich, A. T.; Rauchfuss, T. B.; Strotman, N. A.; Vojvodic, A.; Ward, T. R.; Yang, J. Y.; Surendranath, Y. Using nature's blueprint to expand catalysis with Earth-abundant metals. *Science* **2020**, *369* (6505), No. eabc3183.

(17) Kinzel, N. W.; Werlé, C.; Leitner, W. Transition Metal Complexes as Catalysts for the Electroconversion of CO2: An Organometallic Perspective. *Angew. Chem., Int. Ed.* **2021**, *60* (21), 11628−11686.

(18) Mondal, B.; Neese, F.; Ye, S. Control in the Rate-Determining Step Provides a Promising Strategy To Develop New Catalysts for CO2 Hydrogenation: A Local Pair Natural Orbital Coupled Cluster Theory Study. *Inorg. Chem.* **2015**, *54* (15), 7192−7198.

(19) Mondal, B.; Neese, F.; Ye, S. Toward Rational Design of 3d Transition Metal Catalysts for CO2 Hydrogenation Based on Insights into Hydricity-Controlled Rate-Determining Steps. *Inorg. Chem.* **2016**, *55* (11), 5438−5444.

(20) Ceballos, B. M.; Yang, J. Y. Directing the reactivity of metal hydrides for selective CO2 reduction. *Proc. Natl. Acad. Sci. U. S. A.* **2018**, *115* (50), 12686−12691.

(21) Waldie, K. M.; Ostericher, A. L.; Reineke, M. H.; Sasayama, A. F.; Kubiak, C. P. Hydricity of Transition-Metal Hydrides: Thermodynamic Considerations for CO2 Reduction. *ACS Catal.* **2018**, *8* (2), 1313−1324.

(22) Waldie, K. M.; Brunner, F. M.; Kubiak, C. P. Transition Metal Hydride Catalysts for Sustainable Interconversion of CO2 and Formate: Thermodynamic and Mechanistic Considerations. *ACS Sustainable Chem. Eng.* **2018**, *6* (5), 6841−6848.
(23) Fujita, E.; Creutz, C.; Sutin, N.; Szalda, D. J. Carbon dioxide activation by cobalt(I) macrocycles: factors affecting carbon dioxide and carbon monoxide binding. *J. Am. Chem. Soc.* **1991**, *113* (1), 343−353.
(24) Rozenel, S. S.; Kerr, J. B.; Arnold, J. Metal complexes of Co, Ni and Cu with the pincer ligand HN(CH2CH2PiPr2)2: preparation, characterization and electrochemistry. *Dalton Trans.* **2011**, *40* (40), 10397−10405.
(25) Elgrishi, N.; Chambers, M. B.; Artero, V.; Fontecave, M. Terpyridine complexes of first row transition metals and electrochemical reduction of CO2 to CO. *Phys. Chem. Chem. Phys.* **2014**, *16* (27), 13635−13644.
(26) Lescot, C.; Savourey, S.; Thuéry, P.; Lefèvre, G.; Berthet, J.-C.; Cantat, T. Synthesis, Structure and Electrochemical Behavior of New RPONOP (R = tBu, iPr) Pincer Complexes of Fe2+, Co2+, Ni2+, and Zn2+ ions. *C. R. Chim.* **2016**, *19* (1), 57−70.
(27) Talukdar, K.; Issa, A.; Jurss, J. W. Synthesis of a Redox-Active NNP-Type Pincer Ligand and Its Application to Electrocatalytic CO2 Reduction with First-Row Transition Metal Complexes. *Front. Chem.* **2019**, *7* (330). DOI: 10.3389/fchem.2019.00330
(28) Chatterjee, B.; Chang, W.-C.; Jena, S.; Werlé, C. Implementation of Cooperative Designs in Polarized Transition Metal Systems—Significance for Bond Activation and Catalysis. *ACS Catal.* **2020**, *10* (23), 14024−14055.
(29) Chatterjee, B.; Chang, W. C.; Werlé, C. Molecularly Controlled Catalysis − Targeting Synergies Between Local and Non-local Environments. *ChemCatChem* **2021**, *13*, 1659−1682.
(30) Queyriaux, N. Redox-Active Ligands in Electroassisted Catalytic H+ and CO2 Reductions: Benefits and Risks. *ACS Catal.* **2021**, *11* (7), 4024−4035.
(31) Loipersberger, M.; Cabral, D. G. A.; Chu, D. B. K.; Head-Gordon, M. Mechanistic Insights into Co and Fe Quaterpyridine-Based CO2 Reduction Catalysts: Metal−Ligand Orbital Interaction as the Key Driving Force for Distinct Pathways. *J. Am. Chem. Soc.* **2021**, *143* (2), 744−763.
(32) Benito-Garagorri, D.; Becker, E.; Wiedermann, J.; Lackner, W.; Pollak, M.; Mereiter, K.; Kisala, J.; Kirchner, K. Achiral and Chiral Transition Metal Complexes with Modularly Designed Tridentate PNP Pincer-Type Ligands Based on N-Heterocyclic Diamines. *Organometallics* **2006**, *25* (8), 1900−1913.
(33) Glatz, M.; Bichler, B.; Mastalir, M.; Stöger, B.; Weil, M.; Mereiter, K.; Pittenauer, E.; Allmaier, G.; Veiros, L. F.; Kirchner, K. Iron(ii) complexes featuring κ3- and κ2-bound PNP pincer ligands − the significance of sterics. *Dalton Trans.* **2015**, *44* (1), 281−294.
(34) Glatz, M.; Holzhacker, C.; Bichler, B.; Mastalir, M.; Stöger, B.; Mereiter, K.; Weil, M.; Veiros, L. F.; Mösch-Zanetti, N. C.; Kirchner, K. FeII Carbonyl Complexes Featuring Small to Bulky PNP Pincer Ligands − Facile Substitution of κ2P,N-Bound PNP Ligands by Carbon Monoxide. *Eur. J. Inorg. Chem.* **2015**, *2015* (30), 5053−5065.
(35) Rao, G. K.; Gorelsky, S. I.; Korobkov, I.; Richeson, D. Coinage metal complexes supported by a "PN3P" scaffold. *Dalton Trans.* **2015**, *44*, 19153−19162.
(36) Rösler, S.; Obenauf, J.; Kempe, R. A Highly Active and Easily Accessible Cobalt Catalyst for Selective Hydrogenation of C═O Bonds. *J. Am. Chem. Soc.* **2015**, *137* (25), 7998−8001.
(37) Mastalir, M.; Glatz, M.; Stöger, B.; Weil, M.; Pittenauer, E.; Allmaier, G.; Kirchner, K. Synthesis, characterization and reactivity of vanadium, chromium, and manganese PNP pincer complexes. *Inorg. Chim. Acta* **2017**, *455*, 707−714.
(38) Crystallographic data for the $[Zn(PN_3P)Cl_2]$ complex were not available. Rao, G. K.; Pell, W.; Gabidullin, B.; Korobkov, I.; Richeson, D. Electro- and Photocatalytic Generation of H2 Using a Distinctive CoII "PN3P" Pincer Supported Complex with Water or Saturated Saline as a Hydrogen Source. *Chem. - Eur. J.* **2017**, *23* (66), 16763−16767.
(39) Arevalo, R.; Chirik, P. J. Enabling Two-Electron Pathways with Iron and Cobalt: From Ligand Design to Catalytic Applications. *J. Am. Chem. Soc.* **2019**, *141* (23), 9106−9123.
(40) Wagaw, S.; Buchwald, S. L. The Synthesis of Aminopyridines: A Method Employing Palladium-Catalyzed Carbon−Nitrogen Bond Formation. *J. Org. Chem.* **1996**, *61* (21), 7240−7241.
(41) Addison, A. W.; Rao, T. N.; Reedijk, J.; van Rijn, J.; Verschoor, G. C. Synthesis, structure, and spectroscopic properties of copper(II) compounds containing nitrogen−sulphur donor ligands; the crystal and molecular structure of aqua[1,7-bis(N-methylbenzimidazol-2′-yl)-2,6-dithiaheptane]copper(II) perchlorate. *J. Chem. Soc., Dalton Trans.* **1984**, *7*, 1349−1356.
(42) Garbe, M.; Junge, K.; Beller, M. Homogeneous Catalysis by Manganese-Based Pincer Complexes. *Eur. J. Org. Chem.* **2017**, *2017* (30), 4344−4362.
(43) Jean, Y. *Molecular Orbitals of Transition Metal Complexes*; Oxford University Press: New York, 2005.
(44) Malachowski, M. R.; Adams, M.; Elia, N.; Rheingold, A. L.; Kelly, R. S. Enforcing geometrical constraints on metal complexes using biphenyl-based ligands: spontaneous reduction of copper(II) by sulfur-containing ligands. *J. Chem. Soc., Dalton Trans.* **1999**, No. 13, 2177−2182.
(45) Su, C.-Y.; Liao, S.; Wanner, M.; Fiedler, J.; Zhang, C.; Kang, B.-S.; Kaim, W. The copper(i)/copper(ii) transition in complexes with 8-alkylthioquinoline based multidentate ligands. *Dalton Trans.* **2003**, *2*, 189−202.
(46) Fedorova, O. A.; Shepel, N. E.; Tokarev, S. D.; Lukovskaya, E. V.; Sotnikova, Y. A.; Moiseeva, A. A.; D'Aléo, A.; Fages, F.; Maurel, F.; Fedorov, Y. V. Intramolecular electron transfer in Cu(ii) complexes with aryl-imidazo-1,10-phenanthroline derivatives: experimental and quantum chemical calculation studies. *New J. Chem.* **2019**, *43* (6), 2817−2827.
(47) Kumari, S.; Muthuramalingam, S.; Dhara, A. K.; Singh, U. P.; Mayilmurugan, R.; Ghosh, K. Cu(i) complexes obtained via spontaneous reduction of Cu(ii) complexes supported by designed bidentate ligands: bioinspired Cu(i) based catalysts for aromatic hydroxylation. *Dalton Trans.* **2020**, *49* (39), 13829−13839.
(48) Bocian, A.; Brykczyńska, D.; Kubicki, M.; Hnatejko, Z.; Wałęsa-Chorab, M.; Gorczyński, A.; Patroniak, V. Complexation behavior of 6,6″-dimethyl-2,2′:6′,2″-terpyridine ligand with Co(II), Au(III), Ag(I), Zn(II) and Cd(II) ions: Synthesis, spectroscopic characterization and unusual structural motifs. *Polyhedron* **2019**, *157*, 249−261.
(49) Machan, C. W.; Kubiak, C. P. Electrocatalytic reduction of carbon dioxide with Mn(terpyridine) carbonyl complexes. *Dalton Trans.* **2016**, *45* (43), 17179−17186.
(50) Queyriaux, N.; Abel, K.; Fize, J.; Pécaut, J.; Orio, M.; Hammarström, L. From non-innocent to guilty: on the role of redox-active ligands in the electro-assisted reduction of CO2 mediated by a cobalt(ii)-polypyridyl complex. *Sustain. Energy Fuels* **2020**, *4* (7), 3668−3676.
(51) Savéant, J.-M.; Costentin, C. *Elements of Molecular and Biomolecular Electrochemistry*, 2nd ed.; John Wiley & Sons Inc., 2019; p 86.
(52) Arora, H.; Philouze, C.; Jarjayes, O.; Thomas, F. CoII, NiII, CuII and ZnII complexes of a bipyridine bis-phenol conjugate: Generation and properties of coordinated radical species. *Dalton Trans.* **2010**, *39* (42), 10088−10098.
(53) Wu, Y.; Jiang, J.; Weng, Z.; Wang, M.; Broere, D. L. J.; Zhong, Y.; Brudvig, G. W.; Feng, Z.; Wang, H. Electroreduction of CO2 Catalyzed by a Heterogenized Zn−Porphyrin Complex with a Redox-Innocent Metal Center. *ACS Cent. Sci.* **2017**, *3* (8), 847−852.
(54) Ahmed, M. E.; Rana, A.; Saha, R.; Dey, S.; Dey, A. Homogeneous Electrochemical Reduction of CO2 to CO by a Cobalt Pyridine Thiolate Complex. *Inorg. Chem.* **2020**, *59* (8), 5292−5302.
(55) Shannon, R. D. Revised effective ionic radii and systematic studies of interatomic distances in halides and chalcogenides. *Acta Crystallogr., Sect. A: Cryst. Phys., Diffr., Theor. Gen. Crystallogr.* **1976**, *32* (5), 751−767.

(56) Sampson, M. D.; Nguyen, A. D.; Grice, K. A.; Moore, C. E.; Rheingold, A. L.; Kubiak, C. P. Manganese Catalysts with Bulky Bipyridine Ligands for the Electrocatalytic Reduction of Carbon Dioxide: Eliminating Dimerization and Altering Catalysis. *J. Am. Chem. Soc.* **2014**, *136* (14), 5460−5471.
(57) Rao, G. K.; Pell, W.; Korobkov, I.; Richeson, D. Electrocatalytic reduction of CO2 using Mn complexes with unconventional coordination environments. *Chem. Commun.* **2016**, *52* (51), 8010−8013.
(58) Bertini, F.; Glatz, M.; Gorgas, N.; Stöger, B.; Peruzzini, M.; Veiros, L. F.; Kirchner, K.; Gonsalvi, L. Carbon dioxide hydrogenation catalysed by well-defined Mn(i) PNP pincer hydride complexes. *Chem. Sci.* **2017**, *8* (7), 5024−5029.
(59) Kar, S.; Goeppert, A.; Kothandaraman, J.; Prakash, G. K. S. Manganese-Catalyzed Sequential Hydrogenation of CO2 to Methanol via Formamide. *ACS Catal.* **2017**, *7* (9), 6347−6351.
(60) Erken, C.; Kaithal, A.; Sen, S.; Weyhermüller, T.; Hölscher, M.; Werlé, C.; Leitner, W. Manganese-catalyzed hydroboration of carbon dioxide and other challenging carbonyl groups. *Nat. Commun.* **2018**, *9* (1), 4521.
(61) Kumar, A.; Daw, P.; Espinosa-Jalapa, N. A.; Leitus, G.; Shimon, L. J. W.; Ben-David, Y.; Milstein, D. CO2 activation by manganese pincer complexes through different modes of metal−ligand cooperation. *Dalton Trans.* **2019**, *48* (39), 14580−14584.
(62) Su, X.; McCardle, K. M.; Panetier, J. A.; Jurss, J. W. Electrocatalytic CO2 reduction with nickel complexes supported by tunable bipyridyl-N-heterocyclic carbene donors: understanding redox-active macrocycles. *Chem. Commun.* **2018**, *54* (27), 3351−3354.
(63) Su, X.; McCardle, K. M.; Chen, L.; Panetier, J. A.; Jurss, J. W. Robust and Selective Cobalt Catalysts Bearing Redox-Active Bipyridyl-N-heterocyclic Carbene Frameworks for Electrochemical CO2 Reduction in Aqueous Solutions. *ACS Catal.* **2019**, *9* (8), 7398−7408.
(64) Chen, L.; Guo, Z.; Wei, X.-G.; Gallenkamp, C.; Bonin, J.; Anxolabéhère-Mallart, E.; Lau, K.-C.; Lau, T.-C.; Robert, M. Molecular Catalysis of the Electrochemical and Photochemical Reduction of CO2 with Earth-Abundant Metal Complexes. Selective Production of CO vs HCOOH by Switching of the Metal Center. *J. Am. Chem. Soc.* **2015**, *137* (34), 10918−10921.
(65) Lu, C. C.; Saouma, C. T.; Day, M. W.; Peters, J. C. Fe(I)-Mediated Reductive Cleavage and Coupling of CO2: An FeII(μ-O,μ-CO)FeII Core. *J. Am. Chem. Soc.* **2007**, *129* (1), 4−5.
(66) Shaffer, D. W.; Johnson, S. I.; Rheingold, A. L.; Ziller, J. W.; Goddard, W. A.; Nielsen, R. J.; Yang, J. Y. Reactivity of a Series of Isostructural Cobalt Pincer Complexes with CO2, CO, and H+. *Inorg. Chem.* **2014**, *53* (24), 13031−13041.
(67) Chan, C.; Carpenter, A. E.; Gembicky, M.; Moore, C. E.; Rheingold, A. L.; Figueroa, J. S. Associative Ligand Exchange and Substrate Activation Reactions by a Zero-Valent Cobalt Tetraisocyanide Complex. *Organometallics* **2019**, *38* (7), 1436−1444.
(68) Norouziyanlakvan, S.; Rao, G. K.; Ovens, J.; Gabidullin, B.; Richeson, D. Electrocatalytic H2 Generation from Water Relying on Cooperative Ligand Electron Transfer in "PN3P" Pincer-Supported NiII Complexes. *Chem. - Eur. J.* **2021**, *27*, 13518.
(69) Lapointe, S.; Khaskin, E.; Fayzullin, R. R.; Khusnutdinova, J. R. Stable Nickel(I) Complexes with Electron-Rich, Sterically-Hindered, Innocent PNP Pincer Ligands. *Organometallics* **2019**, *38* (7), 1581−1594.
(70) Kim, Y.-E.; Kim, J.; Lee, Y. Formation of a nickel carbon dioxide adduct and its transformation mediated by a Lewis acid. *Chem. Commun.* **2014**, *50* (78), 11458−11461.
(71) Aresta, M.; Gobetto, R.; Quaranta, E.; Tommasi, I. A bonding-reactivity relationship for (carbon dioxide)bis-(tricyclohexylphosphine)nickel: a comparative solid-state-solution nuclear magnetic resonance study (phosphorus-31, carbon-13) as a diagnostic tool to determine the mode of bonding of carbon dioxide to a metal center. *Inorg. Chem.* **1992**, *31* (21), 4286−4290.
(72) Schmidt, M. H.; Miskelly, G. M.; Lewis, N. S. Effects of redox potential, steric configuration, solvent, and alkali metal cations on the binding of carbon dioxide to cobalt(I) and nickel(I) macrocycles. *J. Am. Chem. Soc.* **1990**, *112* (9), 3420−3426.
(73) Kelly, C. A.; Mulazzani, Q. G.; Venturi, M.; Blinn, E. L.; Rodgers, M. A. J. The Thermodynamics and Kinetics of CO2 and H+ Binding to Ni(cyclam)+ in Aqueous Solution. *J. Am. Chem. Soc.* **1995**, *117* (17), 4911−4919.
(74) Morris, A. J.; Meyer, G. J.; Fujita, E. Molecular Approaches to the Photocatalytic Reduction of Carbon Dioxide for Solar Fuels. *Acc. Chem. Res.* **2009**, *42* (12), 1983−1994.
(75) Schneider, J.; Jia, H.; Muckerman, J. T.; Fujita, E. Thermodynamics and kinetics of CO2, CO, and H+ binding to the metal centre of CO2 reduction catalysts. *Chem. Soc. Rev.* **2012**, *41* (6), 2036−2051.
(76) Pavlishchuk, V. V.; Addison, A. W. Conversion constants for redox potentials measured versus different reference electrodes in acetonitrile solutions at 25°C. *Inorg. Chim. Acta* **2000**, *298* (1), 97−102.
(77) Froehlich, J. D.; Kubiak, C. P. Homogeneous CO2 Reduction by Ni(cyclam) at a Glassy Carbon Electrode. *Inorg. Chem.* **2012**, *51* (7), 3932−3934.
(78) Wang, F.; Cao, B.; To, W.-P.; Tse, C.-W.; Li, K.; Chang, X.-Y.; Zang, C.; Chan, S. L.-F.; Che, C.-M. The effects of chelating N4 ligand coordination on Co(ii)-catalysed photochemical conversion of CO2 to CO: reaction mechanism and DFT calculations. *Catal. Sci. Technol.* **2016**, *6* (20), 7408−7420.
(79) Bi, J.; Hou, P.; Liu, F.-W.; Kang, P. Electrocatalytic Reduction of CO2 to Methanol by Iron Tetradentate Phosphine Complex Through Amidation Strategy. *ChemSusChem* **2019**, *12* (10), 2195−2201.
(80) Stanbury, M.; Compain, J.-D.; Chardon-Noblat, S. Electro and photoreduction of CO2 driven by manganese-carbonyl molecular catalysts. *Coord. Chem. Rev.* **2018**, *361*, 120−137.
(81) Fulmer, G. R.; Miller, A. J. M.; Sherden, N. H.; Gottlieb, H. E.; Nudelman, A.; Stoltz, B. M.; Bercaw, J. E.; Goldberg, K. I. NMR Chemical Shifts of Trace Impurities: Common Laboratory Solvents, Organics, and Gases in Deuterated Solvents Relevant to the Organometallic Chemist. *Organometallics* **2010**, *29* (9), 2176−2179.

https://doi.org/10.1021/acs.inorgchem.1c02909
Inorg. Chem. 2021, 60, 19062−19078